Impurity resistivity of the Earth's inner core

Hitoshi Gomi[1] and Kei Hirose[2]

[1]The University of Tokyo
[2]Tokyo Institute of Technology

May 25, 2023

Abstract

Seismic observations suggest that the Earth's inner core has a complex structure (e.g., the isotropic layer at the top, innermost inner core, and hemispherical dichotomy). These characteristics are believed to reflect the history of dynamics and temperature profile of the inner core. One critical physical property is the inner core's thermal conductivity. The thermal conductivity of metals can be estimated from their electrical resistivity using the Wiedemann-Franz law. Recent high-pressure and temperature experiments revealed that the temperature dependence of electrical resistivity is small for Fe-Si alloys. The small temperature coefficient means that it is essential to determine the impurity resistivity of Fe alloys to constrain the inner core's thermal conductivity. Therefore, this study systematically calculated the impurity resistivities of 4- and 6-component alloys at inner core pressure by combining the Korringa-Kohn-Rostoker method with the coherent potential approximation. As a result, we obtained the thermal conductivity of the inner core to be 150-263 W/m/K. The inner core cannot maintain thermal convection with such a high thermal conductivity, resulting in a flat temperature profile. In materials science, it is widely known that polycrystals soften suddenly at high temperatures a few percent below their melting temperature. If such a pre-melting occurs in the inner core, the flat temperature profile due to high thermal conductivity causes variations in the attenuation within the inner core. This may explain the observation that the upper inner core is more strongly attenuated than the innermost inner core.

Hosted file

`963509_0_art_file_10991419_rsphzy.docx` available at https://authorea.com/users/618704/articles/643668-impurity-resistivity-of-the-earth-s-inner-core

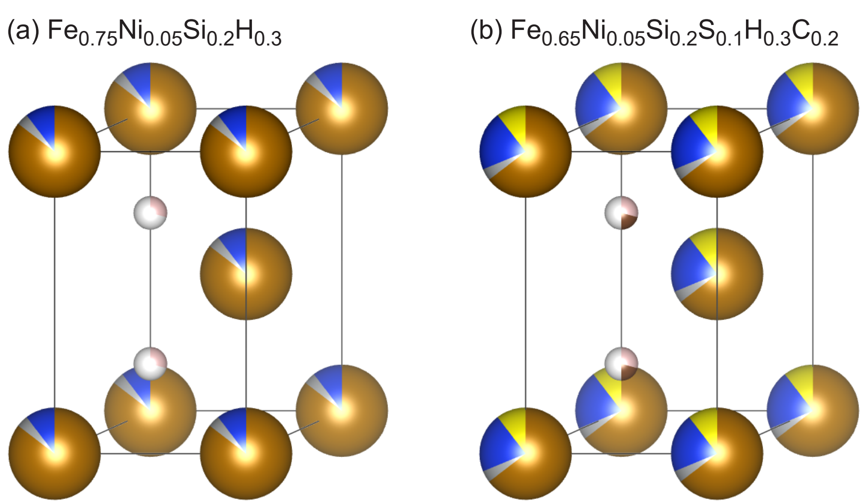

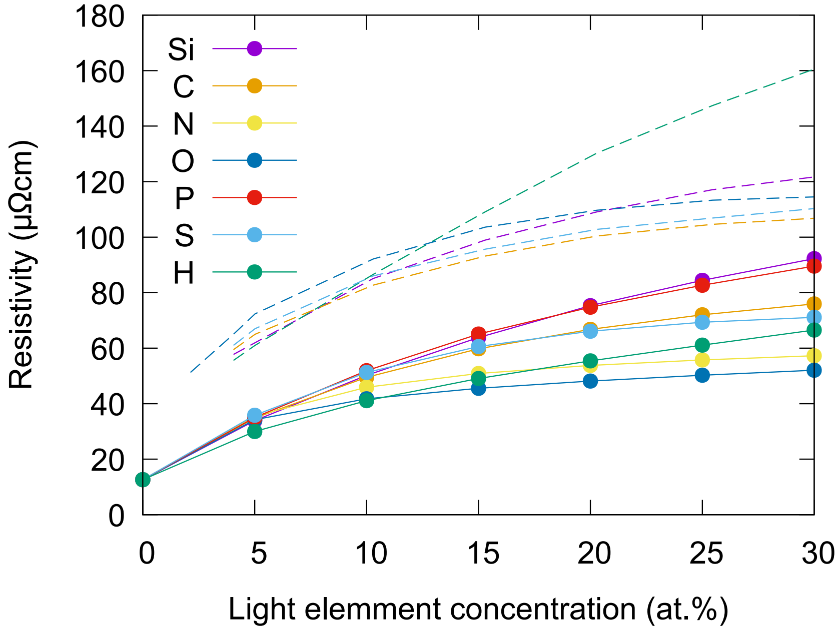

Resistivity (μΩcm)
Light elemment concentration (at.%)
Si
C
N
O
P
S
H
0
20
40
60
80
100
120
140
160
180
0
5
10
15
20
25
30

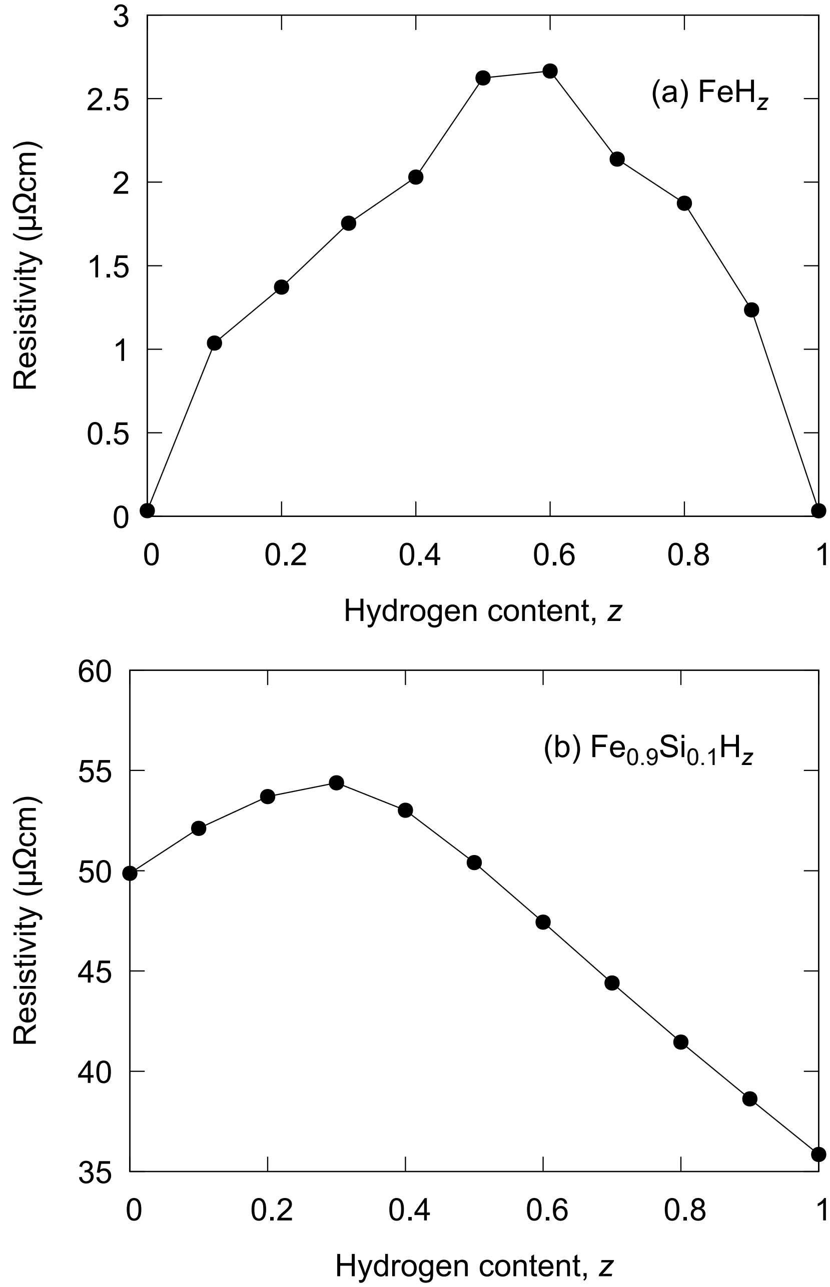
(a) FeH_z
Resistivity (μΩcm)
Hydrogen content, z
(b) $Fe_{0.9}Si_{0.1}H_z$
Resistivity (μΩcm)
Hydrogen content, z

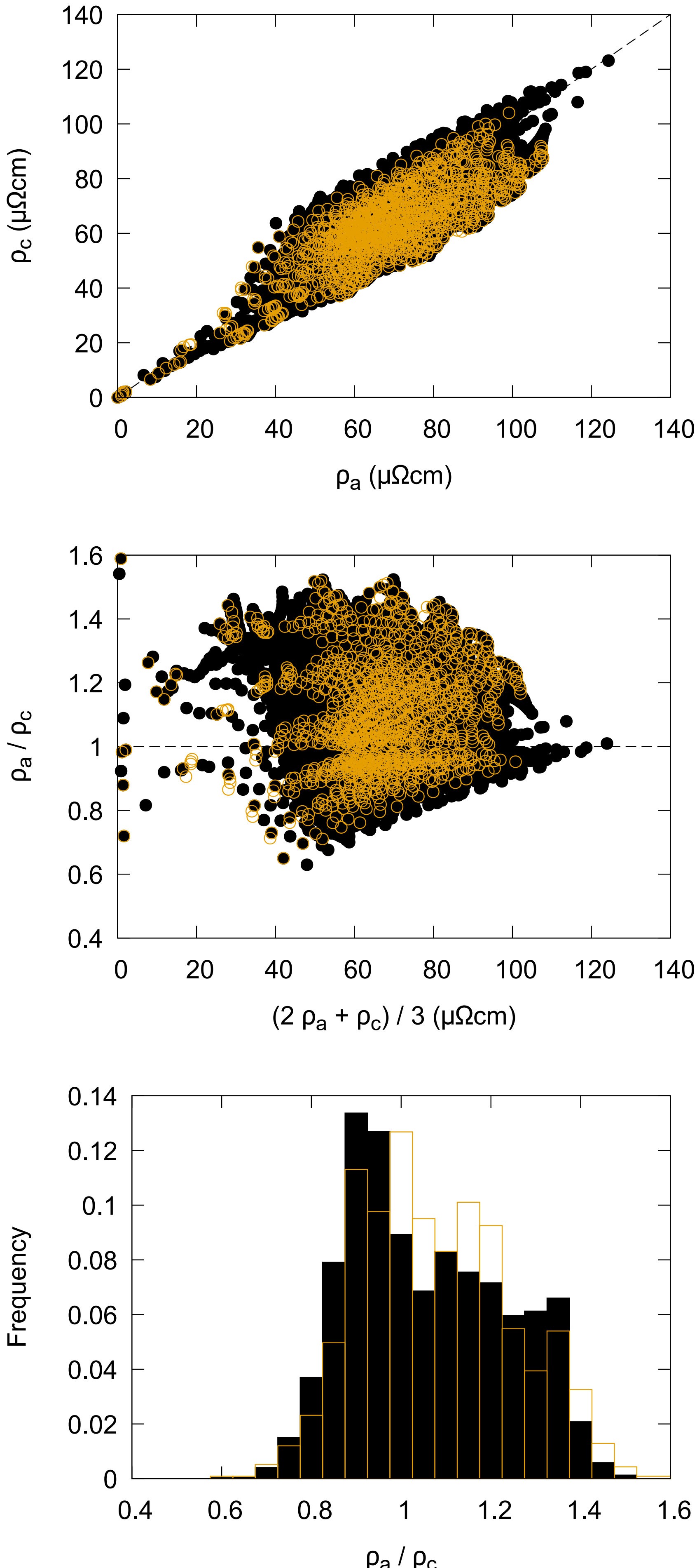
140
120
100
80
60
40
20
0
ρc (μΩcm)
0 20 40 60 80 100 120 140
ρa (μΩcm)
1.6
1.4
1.2
1
0.8
0.6
0.4
ρa / ρc
0 20 40 60 80 100 120 140
(2 ρa + ρc) / 3 (μΩcm)
0.14
0.12
0.1
0.08
0.06
0.04
0.02
0
Frequency
0.4 0.6 0.8 1 1.2 1.4 1.6
ρa / ρc

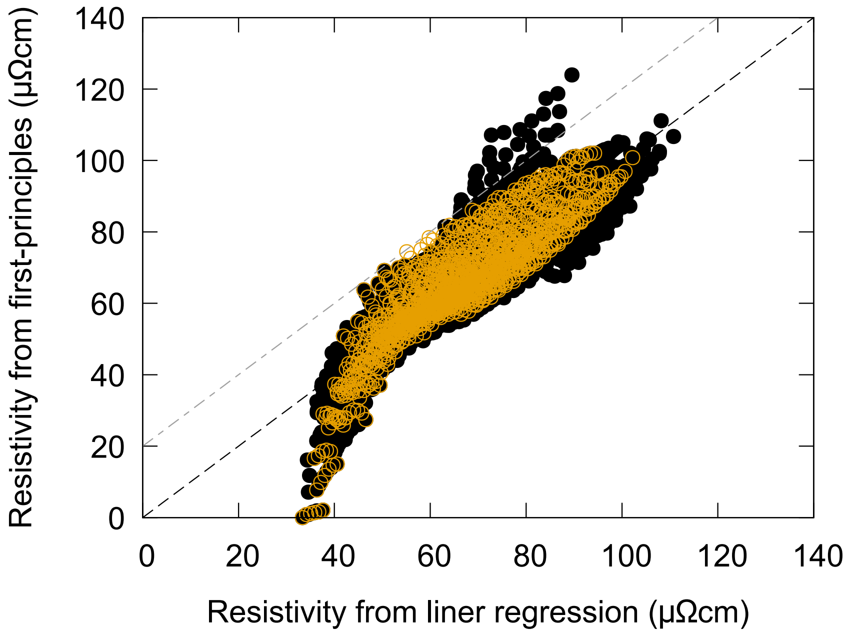
Resistivity from first-principles (μΩcm)
Resistivity from liner regression (μΩcm)
0
20
40
60
80
100
120
140

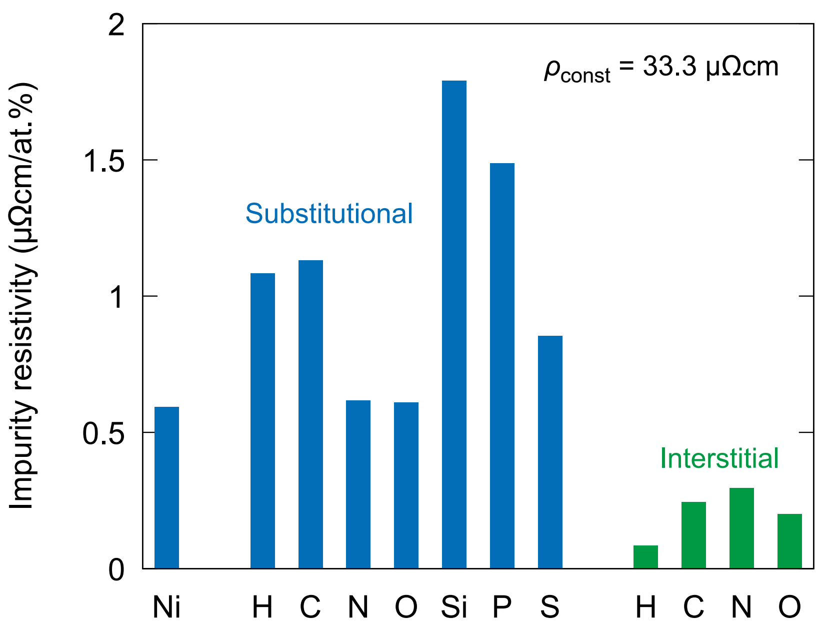
Impurity resistivity (μΩcm/at.%)
ρ_{const} = 33.3 μΩcm
Substitutional
Interstitial
Ni
H
C
N
O
Si
P
S
H
C
N
O
0
0.5
1
1.5
2

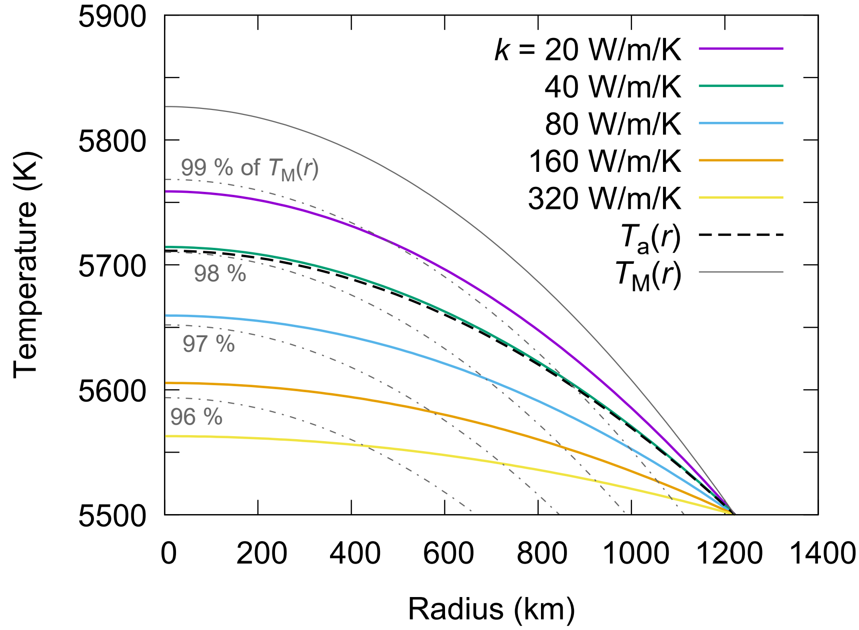

5900
5800
5700
5600
5500
Temperature (K)
0
200
400
600
800
1000
1200
1400
Radius (km)
k = 20 W/m/K
40 W/m/K
80 W/m/K
160 W/m/K
320 W/m/K
Ta(r)
TM(r)
99 % of TM(r)
98 %
97 %
96 %

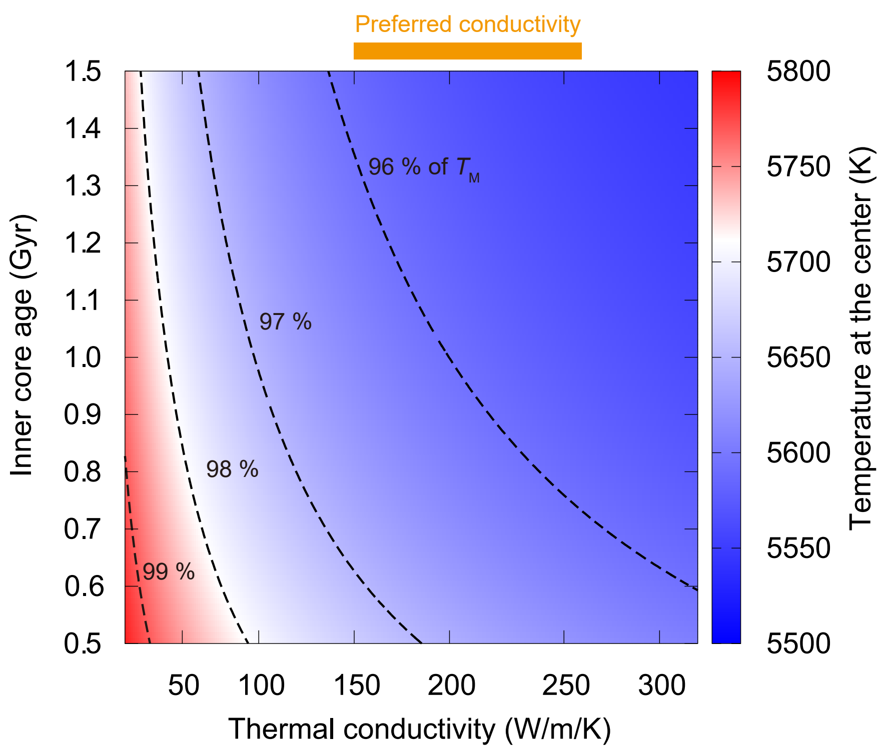

Preferred conductivity
1.5
1.4
1.3
1.2
1.1
1.0
0.9
0.8
0.7
0.6
0.5
Inner core age (Gyr)
50
100
150
200
250
300
Thermal conductivity (W/m/K)
96 % of TM
97 %
98 %
99 %
5800
5750
5700
5650
5600
5550
5500
Temperature at the center (K)

Impurity resistivity of the Earth's inner core

Hitoshi Gomi [a, b] *, Kei Hirose [a, b]

[a] Department of Earth and Planetary Science, The University of Tokyo, 7-3-1 Hongo, Bunkyo, Tokyo, 113-0033, Japan
[b] Earth-Life Science Institute, Tokyo Institute of Technology, 2-12-1 Ookayama, Meguro, Tokyo, 152-8550, Japan

* Corresponding author. *E-mail address*: hitoshi.gomi@eps.s.u-tokyo.ac.jp

Abstract

Seismic observations suggest that the Earth's inner core has a complex structure (e.g., the isotropic layer at the top, innermost inner core, and hemispherical dichotomy). These characteristics are believed to reflect the history of dynamics and temperature profile of the inner core. One critical physical property is the inner core's thermal conductivity. The thermal conductivity of metals can be estimated from their electrical resistivity using the Wiedemann-Franz law. Recent high-pressure and temperature experiments revealed that the temperature dependence of electrical resistivity is small for Fe-Si alloys. The small temperature coefficient means that it is essential to determine the impurity resistivity of Fe alloys to constrain the inner core's thermal conductivity. Therefore, this study systematically calculated the impurity resistivities of 4- and 6-component alloys at inner core pressure by combining the Korringa-Kohn-Rostoker method with the coherent potential approximation. As a result, we obtained the thermal conductivity of the inner core to be 150-263 W/m/K. The inner core cannot maintain thermal convection with such a high thermal conductivity, resulting in a flat temperature profile. In materials science, it is widely known that polycrystals soften suddenly at high temperatures a few percent below their melting temperature. If such a pre-melting occurs in the inner core, the flat temperature profile due to high thermal conductivity causes variations in the attenuation within the inner core. This may explain the observation that the upper inner core is more strongly attenuated than the innermost inner core.

Plain Language Summary

The center of the Earth is an inner core of solid Fe alloy, which has been grown from the surrounding liquid outer core for about one billion years. Therefore, geoscientists regard it as a time capsule that has recorded the history of the Earth. We determined the thermal conductivity of the inner core, which is important for its history, from computer simulations. We found that the thermal conductivity is high, resulting in a small temperature variation of only less than about 100 K within the present-day inner core with a radius of 1,221 km. Because the surface of the inner core is in contact with the liquid outer core, its temperature equals its melting temperature. The temperature difference between the flat profile and the melting curve becomes larger at the deep inner core because the melting temperature increases with pressure. The deviation from the melting temperature may explain the seismic observation that the upper inner core is softer than the innermost inner core due to the effect of pre-melting, which is well-known in material science.

Key points:

- Impurity resistivity of up to 6-component hcp Fe-based alloys are calculated by the KKR-CPA method.
- Linear regression suggests resistivity saturation, leading to the inner core’s high thermal conductivity (150-263 W/m/K).
- A flat temperature profile of the inner core may be across the boundary due to pre-melting consistent with seismic observation.

1. Introduction

At the center of the Earth, there is a solid inner core mainly composed of Fe and Ni alloying with light elements (e.g., Hirose et al., 2021). Even though this inner core is only 0.7% of the Earth's total volume, many characteristic seismic wave observations have been reported (Deguen, 2012; Deuss, 2014). For example, seismic anisotropy and attenuation characterize the uppermost isotropic layer with 60-80 km thick (e.g., Ouzounis & Creager, 2001; Song & Helmberger, 1995), innermost inner core with the radius of 300-600 km (e.g., Cormier & Li, 2002; Cormier & Stroujkova, 2005; Ishii & Dziewonski, 2002; Li & Cormier, 2002; Pham & Tkalčić, 2023; Stephenson et al., 2021), and hemispherical dichotomy (e.g., Tanaka & Hamaguchi, 1997). All these characteristic observations must be simultaneously explained by dynamics and mineralogy. However, to the best of our knowledge, no single model can explain all observations (Deguen, 2012; Deuss, 2014). Several proposed models can independently explain individual seismic features, but some have exclusive relationships. For example, plume convection in the inner core (Jeanloz & Wenk, 1988; Weber & Machetel, 1992) and translation (Alboussiere et al., 2010; Monnereau et al., 2010) cannot exist simultaneously (Lasbleis & Deguen, 2015; Lythgoe et al., 2015). Thermal conductivity is one of the fundamental properties for understanding the dynamics and temperature profile of the inner core (e.g., Labrosse, 2014; Lythgoe et al., 2015; Yukutake, 1998).

The thermal conductivity of metals can be estimated from their electrical resistivity using the Wiedemann-Franz law. Gomi et al. (2013) proposed the model that incorpolate the resistivity saturation (Bohnenkamp et al., 2002; Gunnarsson et al., 2003) to constrain the electrical resistivity of Fe-based alloys at the core conditions. Resistivity saturation predicts that the electrical resistivity of Fe alloys will exhibit a weaker temperature dependence than the linear temperature dependence expected from Bloch-Grüneisen law and Matthiessen's rule (Gomi et al., 2013). The temperature dependence of the electrical resistivity of pure Fe is still under debate, both experimental (Ohta et al., 2016; Suehiro et al., 2019; Zhang et al., 2020a) and theoretical (Kleinschmidt et al., 2023; Pozzo & Alfe, 2016; Ramakrishna et al., 2022; 2023; Xu et al., 2018) studies. Contrary to the discussion of the temperature dependence of resistivity in pure Fe, different experimental groups have independently reported the breakdown of the Matthiessen's rule and small temperature dependence of the resistivity of Fe-Si alloys (Inoue et al., 2020; Zhang et al., 2022). This implies that it is essential to constrain the impurity resistivity in Fe alloys with high impurity content, such as the inner core.

Recently, high-pressure resistivity measurements have been actively reported for binary Fe-based alloys: Ni (Gomi & Hirose, 2015; Lenhart & Secco, 2022; Orole et al., 2022), Si (Berrada et al., 2021; Gomi et al., 2016; Inoue et al., 2020; Zhang et al., 2022), S (Littleton et al., 2021a, b; Manthilake et al., 2019; Pommier, 2018; Pommier et al., 2019), C (Zhang et al., 2018), P (Yin et al., 2020), and H (Ohta et al., 2019). However, the resistivity of multi-component Fe alloys in the Earth's core is difficult to estimate from the binary alloys because of the breakdown of the Mathiesen's rule (Gomi et al., 2016; Gomi & Yoshino, 2018; Inoue et al., 2020; Zhang et al., 2022). Furthermore, experiments on ternary systems are still limited (Berrada et al., 2022; Lenhart et al., 2023; Littleton et al., 2022; Pommier, 2020; Suehiro et al., 2017). In contrast, the coherent potential approximation (CPA) can efficiently compute multi-component alloys. Electrical resistivity of Fe alloys with substitutional impurities has been reported up to ternary systems using the CPA (Gomi et al., 2016; Gomi & Yoshino, 2018; Zidane et al., 2020). These calculations reasonably reproduce the previous experiments using diamond anvil cells (DAC) (Gomi & Hirose, 2015; Gomi et al., 2016; Suehiro et al., 2017; Zhang et al., 2018). Thus, one of the purposes of this study is to calculate the electrical resistivity of Fe-Ni-based alloys with more than two light alloying elements. Another objective of this study is to calculate the electrical resistivity of interstitial impurities, which has yet to be theoretically investigated. Among the light element candidates in the core, H, C, and N may occupy interstitial sites. Gomi et al. (2018) predicted from the band structure of hexagonal close-packed (hcp) and double hexagonal close-packed (dhcp) FeH_x that interstitial H has little effect on electrical resistivity. Also, Ohta et al. (2019) found that the impurity resistivity of H is smaller than the other light element candidates from electrical resistivity measurements of face-centered cubic (fcc) FeH_x at high pressure and temperature using DAC. However, Zidan et al. (2020) calculated the impurity resistivity of hcp Fe alloys with H in the substitutional sites, which exhibit higher than that of other light-element alloys. These results imply that the difference in sites occupied by impurities may significantly affect the electrical resistivity.

In this study, we calculate the impurity resistivity of hcp Fe-based alloys from first-principles calculations up to 6-component with impurities in both substitutional and interstitial sites. Then, we performed linear regression on the obtained electrical resistivity data to confirm the saturation behaviour of resistivity. Finally, the thermal conductivity of the inner core is estimated, and the temperature profile of the inner core is discussed.

2. Methods

2.1 First-principles calculation

Following our previous studies (Gomi et al., 2016; Gomi & Yoshino, 2018), we performed first-principles calculations on hcp Fe-based alloys by using the Korringa-Kohn-Rostoker (KKR) Green function method combined with the coherent potential approximation (CPA), which is implemented in the AkaiKKR (machikaneyama) package (Akai, 1989). The local density approximation (LDA) was used for the exchange-corelation potential (Moruzzi et al., 1978). The crystal potential was approximated by the atomic spherical approximation (ASA). The maximum angular momentum quantum number was set to l = 3. Relativistic effects are treated within the scalar relativistic approximation. The electrical resistivity is calculated from the Kubo-Greenwood formula with the vertex correction (Kou & Akai, 2018; Oshita et al., 2009). Two independent resistivity components were computed with respect to the crystallographic orientation, and the polycrystalline average is calculated as $\rho_{\mathrm{poly}} = (2\rho_{\mathrm{a}} + \rho_{\mathrm{c}})/3$, where ρ_{a} and ρ_{c} are the resistivity component perpendicular and parallel to the c-axis, respectively.

Previous KKR-CPA studies (Gomi et al., 2016; Gomi & Yoshino, 2018; Zidane et al., 2020) have reported calculations of up to ternary systems containing only substitutional impurities. In this study, we calculated up to 6-component alloys containing substitutional and interstitial impurities. The volume is fixed at V = 12.91 Å^3 regardless of composition, which is the volume of hcp Fe at 360 GPa and 300 K (Dewaele et al., 2006). The axial ratio was fixed to the ideal value for hcp metals (c/a = 1.633). First, calculations were performed for Fe-Ni-based substitutional $Fe_{0.9-y}Ni^{s}_{0.1}L^{s}_{y}Vc^{i}_{1.0}$ ternary alloys to check the effect of adding vacancies (Vc) in the interstitial positions. The compositions of the ternary alloys are $Fe_{0.9-y}Ni^{s}_{0.1}L^{s}_{y}Vc^{i}_{1.0}$, where L^{s} is the light element (L^{s} = H, C, N, O, Si, P, or S) and the superscript s indicate the substitutional element. The concentration of substitutional light elements was set with 0.05 steps in the range $0 \leq y \leq 0.3$. Vacancies were introduced at the octahedral interstitial positions. Then, calculations were performed for FeH^{i}_{z} and $Fe_{0.9}Si^{s}_{0.1}H^{i}_{z}$ with H in the interstitial positions. The superscript i means that it is an interstitial element. The H concentration was set to $0.0 \leq z \leq 1.0$. After these test calculations, we computed the 4- and 6-component alloys. The chemical composition of the 4-component alloys can be described as $Fe_{1-x-y}Ni^{s}_{x}L^{s}_{y}L^{i}_{z}$ (Figure 1a), where the substitutional impurities are L^{s} = H, C, N, O, Si, P, or S, and the interstitial impurities are L^{i} = H, C, N, or O. Ni concentrations were set to x = 0, 0.05, 0.1, 0.15. The concentration of the substitutional light element (L^{s}) is set to y = 0, 0.05, 0.1, 0.15, 0.2, 0.25, 0.3. The interstitial impurity (L^{i}) concentration was set to z = 0, 0.05, 0.1, 0.15 0.2, 0.25, 0.3, 0.35, 0.4, 0.5. We successfully obtained 6105 independent chemical compositions. We further calculated the 6-component alloys, $Fe_{1-x-y}Ni^{s}_{x}(Si, S)^{s}_{y}(H, C)^{i}_{z}$, in which two light elements are alloyed at the substitutional and interstitial sites, respectively (Figure 1b). The Si (y_{Si}) and S (y_{S}) concentrations at the substitution sites were varied in 0.05 steps in the range where the sum $y = y_{Si} + y_{S}$ is $y \leq 0.3$. Similarly, the H (z_{H}) and C (z_{C}) concentrations at the interstitial sites were varied in 0.1 steps so that the sum $z = z_H + z_C \leq 0.5$. As a result, 1176 independent compositions were obtained for 6-component alloys.

2.2 Linear regression

We performed linear regression on the resistivities of 6105 compositions obtained from the resistivity calculations of 4-component alloys. If the effect of resistivity saturation is small, the electrical resistivity of multi-component alloys follows Mathiesen's rule.

$$\rho = x\rho_{\mathrm{Ni^s}} + \sum_{\mathrm{L^s}}^{\mathrm{H,C,N,O,Si,P,S}} y_{\mathrm{L^s}}\rho_{\mathrm{L^s}} + \sum_{\mathrm{L^i}}^{\mathrm{H,C,N,O}} z_{\mathrm{L^i}}\rho_{\mathrm{L^i}} \quad (1)$$

Therefore, we considered Matthiesen's rule with a constant term as a linear regression model in this study.

$$\rho = x\rho_{\mathrm{Ni^s}} + \sum_{\mathrm{L^s}}^{\mathrm{H,C,N,O,Si,P,S}} y_{\mathrm{L^s}}\rho_{\mathrm{L^s}} + \sum_{\mathrm{L^i}}^{\mathrm{H,C,N,O}} z_{\mathrm{L^i}}\rho_{\mathrm{L^i}} + \rho_{\mathrm{const}} \quad (2)$$

where the explanatory variables are the concentration of each impurity (x, $y_{\mathrm{L}}^{\mathrm{s}}$, and $z_{\mathrm{L}}^{\mathrm{i}}$), and the regression coefficients are the impurity resistivity ($\rho_{\mathrm{Ni}}^{\mathrm{s}}$, $\rho_{\mathrm{L}}^{\mathrm{s}}$, $\rho_{\mathrm{L}}^{\mathrm{i}}$) and the constant term ρ_{const}.

2.3 Thermal conductivity of the inner core

The temperature dependence of resistivity is small for alloys with large impurity resistivity, such as Fe-Si alloys (Inoue et al., 2020; Zhang et al., 2022). In such cases, the contribution of lattice vibrations to the total resistivity should be small. Thus, Zidane et al. (2020) ignore it. However, in the case of alloys low impurity resistivity (e.g., interstitial H), ignoring the contribution of lattice vibrations may overestimate the thermal conductivity of the inner core. Therefore, following our previous studies (Gomi et al., 2016; Gomi & Yoshino, 2019), we incorporated the effect of lattice vibration on the impurity resistivity obtained from first-principles calculations. The resistivity of hcp Fe at ambient temperature can be described as follows (Gomi et al., 2013).

$$\rho_{\mathrm{Fe}}(V) = 0.526 \times \left(1.24 - \frac{V}{V_0}\right)^{-3.21} \quad \mu\Omega\mathrm{cm} \tag{3}$$

The ideal resistivity at high temperature can be obtained from the Bloch-Grüneisen law.

$$\rho_{\mathrm{Fe,ideal}}(V,T) = B(V)\left(\frac{T}{\Theta_D(V)}\right)^5 \int_0^{\Theta_D(V)/T} \frac{x^5 \mathrm{d}x}{(\exp(x)-1)(1-\exp(-x))} \tag{4}$$

where $B(V)$ is a material constnat obtained from Equation (3), $\Theta_{\mathrm{D}}(V)$ is the Deby temperature (Dewaele et al., 2006). However, note that the resistivity of hcp Fe-based alloys saturate at high temperatures (Inoue et al., 2020; Ohta et al., 2016; Suehiro et al., 2019). The saturation resistivity may be calculated by using the following equation with the ambient pressure value $\rho_{\mathrm{sat}}(V_0)$ = 168 μΩcm (Bohnenkamp et al., 2002) (Gomi et al., 2013).

$$\rho_{\mathrm{sat}}(V) = \rho_{\mathrm{sat}}(V_0)\left(\frac{V}{V_0}\right)^{\frac{1}{3}} \tag{5}$$

This volume dependence is consistent with recent experiments on hcp Fe-Si alloys (Inoue et al., 2020). Several models have been proposed to describe resistivity saturation at ambient pressure, but no universal one is known (Sundqvist, 2022). In this study, we adopted the model of Cote and Meisel (1978) following our previous studies (Gomi et al., 2016; Gomi & Yoshino, 2018). This model fits well with the resistivity of hcp Fe-Si alloys at high pressures and temperatures (Inoue et al., 2020).

$$\rho_{\mathrm{tot}}(V,T) = \left(1 - \frac{\rho_{\mathrm{tot}}(V,T)}{\rho_{\mathrm{sat}}(V)}\right)\rho_{\mathrm{Fe,ideal}}(V,T) + \rho_{\mathrm{poly}} \exp\left(-2W(V,T)\right) \tag{6}$$

$W(V, T)$ can be calculated by the Debye model as follows (Markowitz et al., 1977).

$$W(V,T) = \frac{3\hbar^2 K^2 T^2}{2mk_B\Theta_D^3} \int_0^{\Theta_D(V)/T} \left(\frac{1}{\exp(z)-1} + \frac{1}{2}\right) z \mathrm{d}z \tag{7}$$

where ρ_{poly} is the polycrystalline average of impurity resistivity obtained from present first-principles calculations, $\hbar$ is the reduced Plank's constant (the Dirac's constant), m is the average atomic mass, $K \sim \pi/a$ is electronic wave vector transfer, and a is the lattice parameter. We estimated the thermal conductivity via the Wiedeman-Franz law.

$$k(V,T) = \frac{L_{\mathrm{Somm}}T}{\rho_{\mathrm{tot}}(V,T)} \tag{8}$$

Sommerfeld's value L_{Somm} is widely known as an approximation of the Lorenz number.

$$L_{\mathrm{Somm}} = \frac{\pi^2}{3}\left(\frac{k_B}{e}\right)^2 \tag{9}$$

Although the Lorentz number of Fe alloys at high pressure and temperatures may deviate from L_{Somm} (Gomi & Hirose, 2015; Kleinschmidt et al., 2023; Pourovskii et al., 2017), we use L_{Somm} as a representative value.

2.4 Conductive temperature profile of the inner core

Buffett (2009) modeled the temperature profile due to thermal conduction within the inner core as a function of radial position r and time t from the onset of the inner core. This study uses this model to calculate the present-day conductive temperature profile. The density of the inner core is assumed to depend only on the radial position r, using the polynomial reported by the Preliminary Reference Earth model (PREM) (Dziewonski & Anderson, 1981). In this subsection, we use $\rho(r)$ as the density of the inner core. Note that it is not the electrical resistivity. The radius of the inner core, $r_{\mathrm{ICB}}(t)$, is assumed to be proportional to 1/2 power of time (Buffett, 2009; Labrosse, 2014).

$$r_{\mathrm{ICB}}(t) = r_{\mathrm{ICB}p}\left(\frac{t}{t_{\mathrm{IC}}}\right)^{\frac{1}{2}} \tag{10}$$

where $r_{\mathrm{ICB}p}$ = 1221.5 km is the current radius of the inner core and t_{IC} is the age of the inner core. The inner-core boundary (ICB) temperature always coincides with the melting temperature of the inner core material at that radial position $T_{\mathrm{M}}(r)$, which is modeled based on Lindemann's melting law as follows (Yukutake, 1998).

$$T_M(r) = T_{\mathrm{ICB}p}\left(\frac{\rho_{\mathrm{ICB}}}{\rho(r)}\right)^{\frac{2}{3}} \exp\left[2\gamma\left(1-\frac{\rho_{\mathrm{ICB}p}}{\rho(r)}\right)\right] \tag{11}$$

where $T_{\mathrm{ICB}p}$ = 5500 K is the present-day ICB temperature (Labrosse, 2014), $\rho_{\mathrm{ICB}p}$ $=\rho(r_{\mathrm{ICB}p})$ is the present-day ICB density, γ = 1.5 (Vočadlo et al., 2003) is the Grüneisen parameter. The adiabatic temperature profile can be obtained with the ICB temperature $T_{\mathrm{M}}(r_{\mathrm{ICB}}(t))$ as a reference.

$$T_a(r,t) = T_M\left(r_{\mathrm{ICB}}(t)\right)\left(\frac{\rho(r)}{\rho\left(r_{\mathrm{ICB}}(t)\right)}\right)^{\gamma} \tag{12}$$

The thermal diffusion time $t_{\mathrm{d}}(t)$ is represented as a function of time t via the inner core radius $r_{\mathrm{ICB}}(t)$.

$$t_d(t) = \frac{r_{\mathrm{ICB}}^2(t)}{\kappa} \tag{13}$$

where κ is the thermal diffusivity. For simplicity, the physical properties associated with thermal diffusivity are approximated as independent of radial position r and time t.

$$\kappa = \frac{k}{\rho_{\mathrm{average}} C_P} \tag{14}$$

where k is the thermal conductivity, C_P = 750 J/K/kg is the heat capacity (Gubbins et al., 2013), and ρ_{average} is the average density of the present-day inner core (Dziewonski & Anderson, 1981). Finally, the conductive temperature profile is expressed as follow (Buffett, 2009).

$$T_{\mathrm{cond}}(r,t) = T_M\left(r_{\mathrm{ICB}}(t)\right) + \frac{T_M(0)-T_M\left(r_{\mathrm{ICB}}(t)\right)}{1+\frac{6t_{IC}}{t_d(t)}}\left[1-\left(\frac{r}{r_{\mathrm{ICB}}(t)}\right)^2\right] \tag{15}$$

3. Results

Figure 2 shows the resistivity results at 0 K for the $Fe_{0.9-y}Ni^{s}_{0.1}L^{s}_{y}$ substitutional alloys obtained from first-principles calculations. The electrical resistivity increased with increasing concentration of substitutional impurities. Si had the most significant effect among the substitutional elements investigated in this study, followed by P and C. Compared with a previous study of hcp $Fe_{0.9-y}Ni^{s}_{0.1}L^{s}_{y}$ (Zidane et al., 2020), the present resistivity is smaller than their values. Zidane et al. (2020) report the axial ratio of hcp Fe-based alloys to be $c/a \sim 1$. However, this value is unrealistically small for metals with hcp structure; their failure to optimize c/a may cause such an overestimation of the resistivity. Zidane et al. (2020) also reported higher impurity resistivity for H compared to other light elements. However, the results of this study show that the impurity resistivity of H at substitutional sites is comparable to that of other light elements.

Figure 3(a) shows the resistivity of hcp FeH_z with H occupying the interstitial sites. The compositional dependence of resistivity is concave-down; zero impurity resistivity at $z = 0$ and 1.0, where no chemical disorder exists, and a maximum resistivity around $y = 0.5$ (Figure 3a), consistent with Nordheim's law. However, the resistivity obtained is less than 3 μΩcm, about one order of magnitude smaller than the resistivity of substitutional H (Figure 2). This is because the electrical resistivity of metals is associated with the band broadening due to impurity scattering (Butler, 1985); The local density of states of interstitial H is far below the Fermi level, so the band structure near the Fermi level cannot be affected by H (Gomi et al., 2018). Based on this, Gomi et al. (2018) claimed that the impurity resistivity of FeH_z alloys is almost zero. The present calculations are consistent with this prediction.

Figure 3(b) shows the calculated impurity resistivity of the hcp $Fe_{0.9}Si_{0.1}H_z$ alloy. Due to Si-induced impurity resistivity, the resistivity is not zero even at $z = 0$ and 1.0, and the resistivity is higher in $Fe_{0.9}Si_{0.1}$ than in $Fe_{0.9}Si_{0.1}H_{1.0}$. The dependence of resistivity on H concentration shows a concave-down behavior as in the case of FeH_z, but its peak position is around $z = 0.3$. In the high H concentration region ($z > 0.6$), the resistivity is lower than that of the H-free $Fe_{0.9}Si_{0.1}$. Ohta et al. (2019) conducted electrical resistivity measurements of fcc FeH_z alloys at high pressure and temperature. They reported that the resistivity decreases with increasing H concentration in the high H concentration ($z > 0.5$) region. The present calculations and previous experiments (Ohta et al., 2019) show a similar concave-down trend even though the crystal structures, temperatures, pressures, and chemical compositions differ. As we expect similar behavior for other interstitial impurities, in subsequent calculations for 4- and 6-component alloys, we calculated the impurity resistivity only for the compositional range $z \leq 0.5$, where the resistivity is expected to be larger than in $z = 0$.

The resistivity of metals with an hcp structure has two components, parallel (ρ_c) and perpendicular (ρ_a) to the *c*-axis of the crystal. At ambient pressure, hcp Sc has a large anisotropy, with a value of $\rho_a / \rho_c = 2.2$ (Spedding et al., 1971). Balog and Secco (1999) measured anisotropy in resistivity of hcp Gd up to 1.6 GPa. The anisotropy was $\rho_a / \rho_c = 2.0$ at ambient pressure but decreased linearly with increasing pressure. By extrapolating this trend, they obtained $\rho_a / \rho_c = 1$ at 20.5 GPa. In contrast, Ohta et al. (2018) pointed out the presence of high anisotropy in the thermal conductivity measurements of hcp Fe under high pressure; the value reaches $k_c/k_a = \rho_a / \rho_c = 3$. A similar high anisotropy $\rho_a / \rho_c = 3.03 \pm 0.37$ has also been reported from recent ab initio calculations for hcp Fe (Ramkrishna et al., 2022). The present calculation also demonstrates the anisotropic resistivities (Figure 4a). However, they are relatively moderate compared with previous studies (Ohta et al., 2018; Ramkrishna et al., 2022). Figure 4b plots the resistivity ratio as a function of the polycrystalline average of resistivity. Excluding the low resistivity portion, which is close to zero division, the range of anisotropy is $0.63 \leq \rho_a / \rho_c \leq 1.52$, and strong anisotropy of $\rho_a / \rho_c \sim 3$ was not observed. Figure 4c shows the frequency distribution of resistivity anisotropy. In the composition range investigated in this study, $\rho_a / \rho_c \geq 1$ in most cases, but there were also compositions with $\rho_a / \rho_c \leq 1$.

Gomi et al. (2016) computed Fe-Si, Fe-Ni, and Fe-Ni-Si alloys. They identified three features that indicate saturation of resistivity: (1) bending of the composition dependence of resistivity, (2) smearing of the Bloch spectral function in the vicinity of the Fermi level (where the mean free path is close to the interatomic distance), and (3) a breakdown of Matthiessen's rule. Subsequently, Gomi and Yoshino (2018) calculated resistivities for substitutional binary alloys containing Si and other light elements (H, C, N, O, S), as well as Fe-Si-S ternary alloys. Among the three features due to resistivity saturation shown in Gomi et al. (2016), the broadening of the Bloch spectral function was confirmed by Gomi and Yoshino (2018). However, the presence or absence of resistivity bending is not apparent. Also, the breakdown of Matthiessen's rule was confirmed only for the Fe-Si-S ternary alloys. Therefore, it still needs to be verified for the other multi-component alloys. In this study, linear regression was performed on the calculated resistivity of 4-component alloys (Figure 5) to capture the overall trend of electrical resistivity in multi-component alloys. The regression coefficients were obtained (Figure 6). Among the substitutional impurities, Si exhibits the highest impurity resistivity, while the contribution of Ni is small. This result is consistent with our previous studies (Gomi & Hirose, 2015; Gomi et al., 2016; Gomi & Yoshino, 2018). It is also confirmed that the resistivity of substitutional H is as large as that of other light elements and that the resistivity of interstitial H is much smaller than that of substitutional H. In this study, we used Matthiessen's rule with a constant term as a regression model (Equation 2). If Matthiessen's rule holds for the 4-component alloys we calculated, then the constant term should be zero (or very small). However, this study yielded a huge constant term of 33 μΩcm, meaning Matthiessen's rule has broken down. The reason for the breakdown of Matthiessen's rule can be attributed to the saturation of resistivity. From this perspective, the 4-component alloys in Figure 5 can be divided into three categories. The first is the alloys with the resistivity less than about 40 μΩcm, where the actual resistivity deviates from the linear regression line. In this category, the resistivity is far below the saturation resistivity, and Matthiessen's rule may hold. The second is a category with the resistivity of larger than about 40 μΩcm where a bend in the resistivity trend can be seen and agrees with the linear regression prediction. We considered the resistivity saturation is dominant in this category. The third category is where the actual resistivity is more than ~20 μΩcm higher than the linear regression line. Alloys in this category appears to continue the trend of low resistivity category, which points to the possibility that the compositions in this category become bad metals where resistivity saturation breaks down. If the inner core is a kind of bad metal, then the thermal conductivity of the inner core may be extremely low. Therefore, we looked into the composition of the alloys contained in this category. The alloys in this category were 32 compositions (~5%) out of 6105 total compositions. Twenty compositions contained H in the substitutional sites; the remaining 12 contained O. However, these are unrealistic for the inner core; H tends to occupy the interstitial sites, and O hardly partitions into the solid inner core (Alfe et al., 2002). A more realistic compositions of the core, 6-component (Fe, Ni, Si, S)(H, C) alloys, are also plotted in Figure 5 together with 4-component alloys. Their resistivities are consistent with those of the 4-component alloys. Non of the 6-component alloys have more than ~20 μΩcm large resistivity than the regression line. Therefore, the alloys comprising the inner core are considered to have compositions that follow the standard resistivity saturation.

4. Discussion

The thermal conductivity of the inner core was estimated from the impurity resistivity obtained by first-principles calculations. The thermal conductivities of 6-component $Fe_{1-x-y}Ni^{s}_{x}(Si, S)^{s}_{y}(H, C)^{i}_{z}$ alloys obtained in this study were 120-310 W/m/K at 5500 K. However, some of these 1176 compositions contain too many or too few light elements for the inner core. Therefore, we present the thermal conductivities for five representative compositions. When the only light element in the inner core is interstitial H, the amount of H that satisfies the density of the inner core is about z = 0.22 (Gomi & Hirose, 2022). Considering the 5% of Ni present in the core, the thermal conductivity of $Fe_{0.95}Ni_{0.05}H_{0.2}$ is estimated to be k = 263 W/m/K. Since interstitial H has negligible impurity resistivity, the thermal conductivity of this composition is the upper limit of the thermal conductivity of the inner core. The amount of C required to satisfy the density defects in the inner core is ~1.5 wt.% (Mookherjee et al., 2011) corresponds to about z =

0.07. The thermal conductivity of $Fe_{0.95}Ni_{0.05}C_{0.1}$ is k = 234 W/m/K, which is lower than the H-rich alloy. If all light elements in the inner core were substitutional Si, the concentration would be ~7 wt.%Si (y ~ 0.13) (Tateno et al., 2015). The thermal conductivity of $Fe_{0.8}Ni_{0.05}Si_{0.15}$ is computed to be k = 150 W/m/K. It is reported that the effect of Si and S on the density of hcp Fe alloys is similar (Li et al., 2018). We found that the thermal conductivity of $Fe_{0.8}Ni_{0.05}S_{0.15}$ becomes k = 154 W/m/K, slightly higher than the Si-rich scenario. The thermal conductivity of $Fe_{0.85}Ni_{0.05}Si_{0.05}S_{0.05}H_{0.1}$, as an example with multiple light elements, yielded k = 166 W/m/K. Therefore, for realistic chemical compositions that satisfy the density of the inner core, the range of thermal conductivities would be 150-263 W/m/K. Zidane et al. (2020) estimated the thermal conductivity of the inner core to be 110-155 W/m/K. This value is systematically smaller than this study. The reason may be due to their failure to optimize c/a. Pozzo et al. (2014) obtained a 232 W/m/K thermal conductivity for $Fe_{0.93}Si_{0.07}$. The thermal conductivity of $Fe_{0.95}Si_{0.05}$ obtained from this study, k = 217 W/m/K, is slightly lower than that of Pozzo et al. (2014); Pozzo et al. (2014) reported the Lorentz number as $L = 2.7 \times 10^{-8}$ WΩ/K^2. The difference in thermal conductivity may be because the present study assumes the Sommerfeld value $L_{\mathrm{Somm}} = 2.445 \times 10^{-8}$ WΩ/K^2.

Many characteristic seismic observations (seismic velocity, attenuation, and their anisotropy with depth and hemispherical variations) are known for the Earth’s inner core. However, no single model can explain all of them simultaneously (Deguen, 2012; Deuss, 2014). Among these observations, the innermost inner core is one of the most mysterious to understand from mineralogy and inner core dynamics (Deguen, 2012). The innermost inner core is known as a layer that exists at the center of the inner core with a radius of 300-600 km, which has a different anisotropy (Ishii & Dziewonski, 2002; Pham & Tkalčić, 2023; Stephenson et al., 2021), and a lower attenuation (Cormier & Li, 2002; Cormier & Stroujkova, 2005; Li & Cormier, 2002) than the upper inner core. Buffet (2009) pointed out that the termination of initial thermal convection could form a layer structure in the inner core. However, using recent high thermal conductivity estimates, including this study, thermal convection is impossible even in the initial inner core (Pozzo et al., 2014). Deguen et al. (2018) pointed out that a double-diffusive translation could be terminated at the early stage of the inner core. The following conditions are required for double-diffusion instability (Deguen et al., 2018).

$$-\frac{\alpha\Delta T}{\beta\Delta\chi} \leq Le \tag{16}$$

where $\alpha \sim 10^{-5}$ K^{-1} is the thermal expansion coefficient, $\beta \sim 1$ is the compositional expansion coefficient, $\Delta T \sim$ -100 K is the difference in core center temperature from the adiabatic temperature profile, $\Delta\chi$ is the difference in light element concentration between the center and ICB, and $Le = \kappa/D$ is a dimensionless parameter representing the ratio between thermal diffusivity (κ) and diffusion coefficient (D) of light elements, called Lewis number. With a diffusion coefficient of $D \sim 10^{-12}$ m^2/s for light elements (Gubbins et al., 2013), the Le is calculated to be $\sim 2 \times 10^7$ (Deguen et al., 2018). Due to the huge Le, even with a strong thermal stratification ($\Delta T < 0$), a double-diffusive instability exists if there is a slight compositional instability ($\Delta\chi > 0$) (Deguen et al., 2018). For example, even a slight compositional gradient ($\Delta\chi_O \sim 0.005$ %) (Labrosse, 2014) created by O that is little partitioned into the inner core would result in the left side of Equation (16) being less than 5 (Deguen et al., 2018). Recent ab initio molecular dynamics studies have indicated that interstitial light elements (H, O, and C) may become a superionic state (He et al., 2022). In this case, the diffusion coefficient of these light elements reaches the order of $D \sim 10^{-8}$ m^2/s (He et al., 2022; Wang et al., 2021; Yang et al., 2022), resulting in a Lewis number down to the order of 10^3. However, this value is still sufficiently high for double-diffusive instability. Therefore, the double-diffusive instability is determined only by the sign of $\Delta\chi$. Zhang et al. (2020b) performed atomistic simulations with machine learning potentials to constrain the solid-liquid partitioning of S. Their results show that, in contrast to Gubbins et al. (2013), there is little pressure dependence on the S partition coefficient. If the S concentration in the outer core increases with inner core growth, the S partitioning into the inner core yields compositional stratification ($\Delta\chi_S \leq 0$). The partition coefficient of a light element in a multi-component system may depends on the concentration of the coexisting light element. For example, Hasegawa et al. (2021) conducted high-pressure experiments on a Fe-Si-C system in a DAC. They found that the partition of Si to the solid phase increases with increasing C concentration in the liquid phase. If the core composition can be approxymated by a Fe-Si-C ternary system, the outer core C concentration increases with the inner core growth. In this case, the Si concentration in the inner core also increases toward the top of the core, so Si causes compositional stratification within the inner core ($\Delta\chi_{Si} \leq 0$). It is worth mentioning that, as Deguen et al. (2018) point out, temporal changes in the composition of the liquid reacting with the inner core behave complicated due to the following two reasons; precipitation of MgO and SiO_2 (Badro et al., 2016; Hirose et al., 2017; O'Rourke & Stevenson, 2016) decreases the concentration of light elements in the liquid. Forming a dense layer at the bottom of the outer core makes the composition of the liquid reacting with the inner core depleted in light elements compared with the average composition of the outer core. Thus, early termination of double-diffusive translation is possible for the origin of the innermost inner core. However, in this case, translation cannot explain the hemispherical dichotomy, and other models are needed (e.g. Aubert et al., 2008; Gubbins et al., 2011). Kuwayama et al. (2008) pointed out the possibility of an fcc-hcp phase transition in Fe-Ni alloys within the inner core. In this scenario, the innermost inner core is composed of hcp Fe-Ni alloy, and the upper inner core is fcc. Recently, the possibility of delayed crystallization of the inner core due to super-cooling has been proposed (Huguet et al., 2018). If this is the case, a substantial amount of melt is trapped in the innermost inner core, whereas compaction of a solid matrix extract melts in the upper inner core (Lasbleis et al., 2020). These are the possible origins of the boundary with different physical properties inside the inner core.

In this study, we propose a new mechanism that make a boundary with different physical properites in the inner core due to the pre-melting. Recently, Yamauchi and Takei (2020) reported that the grain boundary pre-melting could explain the sharp lithosphere-asthenosphere boundary observed in the oceanic mantle. The similar bounday is possible in the inner core. Due to grain boundary pre-melting, polycrystals rapidly soften slightly below the melting temperature (e.g., Cantwell et al., 2014). Its characteristic temperature T_{PM} is several percent below the melting temperature (Martorell et al., 2013; Nadal & Poac, 2003; Yamauchi & Takei, 2016). In the polycrystalline Sn experiments by Nadal and Poac (2003), a sharp decrease in shear modulus occurred within 1% of the melting temperature ($T_{PM} > 0.99\ T_M$). Yamauchi and Takei (2016) showed from experiments on polycrystalline Borneol ($C_{10}H_{18}O$), a mantle analog composed of organic materials, that softening occurs at $T_{PM} > 0.92\ T_M$. Martorell et al. (2013) calculated the elastic constants of single-crystal hcp Fe without grain boundaries by using the first principles calculations up to melting temperature at inner core pressure. They found a decrease in the shear modulus at $T_{PM} > 0.96\ T_M$. Martorell et al. (2013) argued that pre-melting occurs throughout the inner core assuming the adiabatic temperature profile. However, suppose the thermal conductivity of the inner core is high and the resultant temperature gradient is flat. In that case, the difference between the melting temperature and core conductive temperature profile increases as one goes deeper into the inner core, and pre-melting may not occur at the center. Figure 7 shows the temperature profile of the inner core as a function of the thermal conductivity with the age of the inner core to be t_{IC} = 1.0 Gyr. The higher the thermal conductivity, the smaller the temperature gradient within the inner core. For the present inner core to be thermally convective, the temperature determined by thermal conduction must be higher than that determined by the adiabatic temperature gradient (Yukutake, 1998). Therefore, the present-day inner core cannot maintain thermal convection if the thermal conductivity is higher than 40 W/m/K. This critical value is much lower than the present estimates (k = 150-263 W/m/K), making the present-day inner core likely to be thermally stable. With such high thermal conductivity, the temperature profile of the inner core would be flat. The temperature difference between the present-day ICB and the center was estimated to be less than 110 K. Let us compare the conductive temperature profiles with the pre-melting temperature. In Figure 7, profiles for 99, 98, 97, and 96% of T_M are plotted in addition to the melting curve. If k = 160 W/m/K, t_{IC} = 1.0 Gyr, and $T_{PM} = 0.97\ T_M$, pre-melting does not occur at radius $r \leq$

600 km in the inner core (Figure 7), which may explain the observation that seismic attenuation is stronger in the upper inner core and weaker at the innermost inner core (Cormier & Li, 2002; Cormier & Stroujkova, 2005; Li & Cormier, 2002). We plotted the temperature at the center of the core as a function of core thermal conductivity and the inner core age (Figure 8). T = 5711 K, calculated from adiabat (Equation 12), is a criterion for thermal instability. Therefore, we plotted the region with T < 5711 K as blue and T > 5711 K as red. In the range of present thermal conductivities, the inner core should be thermally stable, meaning no thermally-driven plume convection or thermally-driven translation. In this situation, the temperature profile of the inner core becomes flat, determined by conduction. Although the T_{PM} of the inner core is currently essentially unconstrained, if the $T_{PM} \sim 0.97\ T_M$, then a boundary due to pre-melting can exist in the inner core. This pre-melting boundary could explain the difference in seismic attenuation between the upper inner core and the innermost inner core (Cormier & Li, 2002; Cormier & Stroujkova, 2005; Li & Cormier, 2002). It should be worth mentioning that this pre-melting model can easily be combined with other models to explain other seismic observations (e.g., double-diffusive translation for hemispherical dichotomy) because it depends only on the present-day temperature profile.

5. Summary and conclusion

We computed the impurity resistivity of hcp Fe-based 4- and 6-component alloys by means of KKR-CPA method combined with the Kubo-Greenwood formula. The results exhibit anisotopy $0.63 \leq \rho_a / \rho_c \leq 1.52$, where ρ_c and ρ_a are resistivities parallel and perpendicular to the c-axis, respectively. Interstitial H contributed little to resistivity, consistent with prior experiments (Ohta et al., 2019). Impurities at substitutional sites showed systematically greater resistivity than impurities at interstitial sites. We performed linear regression on the resistivity of the 4-component alloys. The results show the breakdown of Matthiessen's rule due to resistivity saturation. This trend was also observed for hcp (Fe, Ni, Si, S)(H, C) 6-component alloys, which have a more realistic chemical composition of the inner core. The Wiedemann-Franz law was applied to estimate the thermal conductivity of the inner core to be k = 150-263 W/m/K. This value is systematically higher than the previous calculation (Zidane et al., 2020). With the present thermal conductivity values, we calculated the temperature profile due to thermal conduction in the present-day inner core using the model developed by Buffett (2009). The conductive temperature profile is flat, indicating that the inner core cannot maintain thermal convection. Polycrystalline solids are known to soften rapidly at temperatures above a few percent below the melting temperature due to grain boundary pre-melting (e.g., Nadal & Poac, 2003; Yamauchi & Takei, 2016). When the temperature profile is flat, pre-melting occurs only in the upper inner core. This could explain the observations that the attenuation is stronger in the upper inner core and weaker in the innermost inner core (Cormier & Li, 2002; Cormier & Stroujkova, 2005; Li & Cormier, 2002).

References

Akai, H. (1989). Fast Korringa-Kohn-Rostoker coherent potential approximation and its application to FCC Ni-Fe systems. Journal of Physics: Condensed Matter, 1(43), 8045. https://doi.org/10.1088/0953-8984/1/43/006

Alboussiere, T., Deguen, R., & Melzani, M. (2010). Melting-induced stratification above the Earth’s inner core due to convective translation. Nature, 466(7307), 744-747. https://doi.org/10.1038/nature09257

Alfè, D., Gillan, M. J., & Price, G. D. (2002). Composition and temperature of the Earth’s core constrained by combining ab initio calculations and seismic data. Earth and Planetary Science Letters, 195(1-2), 91-98. https://doi.org/10.1016/S0012-821X(01)00568-4

Aubert, J., Amit, H., Hulot, G., & Olson, P. (2008). Thermochemical flows couple the Earth's inner core growth to mantle heterogeneity. Nature, 454(7205), 758-761. https://doi.org/10.1038/nature07109

Badro, J., Siebert, J., & Nimmo, F. (2016). An early geodynamo driven by exsolution of mantle components from Earth’s core. Nature, 536(7616), 326-328. https://doi.org/10.1038/nature18594

Balog, P. S., & Secco, R. A. (1999). Electrical resistivity anisotropy of Gd at high pressure. physica status solidi (b), 214(2), 357-363. https://doi.org/10.1002/(SICI)1521-3951(199908)214:2%3C357::AID-PSSB357%3E3.0.CO;2-9

Berrada, M., Secco, R. A., & Yong, W. (2021). Adiabatic heat flow in Mercury's core from electrical resistivity measurements of liquid Fe-8.5 wt% Si to 24 GPa. Earth and Planetary Science Letters, 568, 117053. https://doi.org/10.1016/j.epsl.2021.117053

Berrada, M., Secco, R. A., & Yong, W. (2022). Resistivity of solid and liquid Fe–Ni–Si with applications to the cores of Earth, Mercury and Venus. Scientific Reports, 12(1), 9941. https://doi.org/10.1038/s41598-022-14130-z

Bohnenkamp, U., Sandström, R., & Grimvall, G. (2002). Electrical resistivity of steels and face-centered-cubic iron. Journal of applied physics, 92(8), 4402-4407. https://doi.org/10.1063/1.1502182

Buffett, B. A. (2009). Onset and orientation of convection in the inner core. Geophysical Journal International, 179(2), 711-719. https://doi.org/10.1111/j.1365-246X.2009.04311.x

Butler, W. H. (1985). Theory of electronic transport in random alloys: Korringa-Kohn-Rostoker coherent-potential approximation. Physical Review B, 31(6), 3260. https://doi.org/10.1103/PhysRevB.31.3260

Cantwell, P. R., Tang, M., Dillon, S. J., Luo, J., Rohrer, G. S., & Harmer, M. P. (2014). Grain boundary complexions. Acta Materialia, 62, 1-48. https://doi.org/10.1016/j.actamat.2013.07.037

Cormier, V. F., & Li, X. (2002). Frequency-dependent seismic attenuation in the inner core 2. A scattering and fabric interpretation. Journal of Geophysical Research: Solid Earth, 107(B12), ESE-14. https://doi.org/10.1029/2002JB001796

Cormier, V. F., & Stroujkova, A. (2005). Waveform search for the innermost inner core. Earth and Planetary Science Letters, 236(1-2), 96-105. https://doi.org/10.1016/j.epsl.2005.05.016

Cote, P. J., & Meisel, L. V. (1978). Origin of saturation effects in electron transport. Physical Review Letters, 40(24), 1586. https://doi.org/10.1103/PhysRevLett.40.1586

Deguen, R. (2012). Structure and dynamics of Earth's inner core. Earth and Planetary Science Letters, 333, 211-225. https://doi.org/10.1016/j.epsl.2012.04.038

Deguen, R., Alboussière, T., & Labrosse, S. (2018). Double-diffusive translation of Earth's inner core. Geophysical Journal International, 214(1), 88-107. https://doi.org/10.1093/gji/ggy120

Deuss, A. (2014). Heterogeneity and anisotropy of Earth's inner core. Annual Review of Earth and Planetary Sciences, 42, 103-126. https://doi.org/10.1146/annurev-earth-060313-054658

Dewaele, A., Loubeyre, P., Occelli, F., Mezouar, M., Dorogokupets, P. I., & Torrent, M. (2006). Quasihydrostatic equation of state of iron above 2 Mbar. Physical Review Letters, 97(21), 215504. https://doi.org/10.1103/PhysRevLett.97.215504

Dziewonski, A. M., & Anderson, D. L. (1981). Preliminary reference Earth model. Physics of the earth and planetary interiors, 25(4), 297-356. https://doi.org/10.1016/0031-9201(81)90046-7

Gomi, H., & Hirose, K. (2015). Electrical resistivity and thermal conductivity of hcp Fe–Ni alloys under high pressure: Implications for thermal convection in the Earth's core. Physics of the Earth and Planetary Interiors, 247, 2-10. https://doi.org/10.1016/j.pepi.2015.04.003

Gomi, H., & Hirose, K. (2022). Magnetism and equation of states of fcc FeH_x at high pressure. American Mineralogist. https://doi.org/10.2138/am-2022-8452

Gomi, H., & Yoshino, T. (2018). Impurity resistivity of fcc and hcp Fe-based alloys: thermal stratification at the top of the core of super-Earths. Frontiers in Earth Science, 6, 217. https://doi.org/10.3389/feart.2018.00217

Gomi, H., Fei, Y., & Yoshino, T. (2018). The effects of ferromagnetism and interstitial hydrogen on the equation of states of hcp and dhcp FeH_x: Implications for the Earth's inner core age. American Mineralogist: Journal of Earth and Planetary Materials, 103(8), 1271-1281. https://doi.org/10.2138/am-2018-6295

Gomi, H., Hirose, K., Akai, H., & Fei, Y. (2016). Electrical resistivity of substitutionally disordered hcp Fe–Si and Fe–Ni alloys: Chemically-induced resistivity saturation in the Earth's core. Earth and Planetary Science Letters, 451, 51-61. https://doi.org/10.1016/j.epsl.2016.07.011

Gomi, H., Ohta, K., Hirose, K., Labrosse, S., Caracas, R., Verstraete, M. J., & Hernlund, J. W. (2013). The high conductivity of iron and thermal evolution of the Earth's core. Physics of the Earth and Planetary Interiors, 224, 88-103. https://doi.org/10.1016/j.pepi.2013.07.010

Gubbins, D., Alfe, D., & Davies, C. J. (2013). Compositional instability of Earth's solid inner core. Geophysical Research Letters, 40(6), 1084-1088. https://doi.org/10.1002/grl.50186

Gubbins, D., Sreenivasan, B., Mound, J., & Rost, S. (2011). Melting of the Earth's inner core. Nature, 473(7347), 361-363. https://doi.org/10.1038/nature10068

Gunnarsson, O., Calandra, M., & Han, J. E. (2003). Colloquium: Saturation of electrical resistivity. Reviews of Modern Physics, 75(4), 1085. https://doi.org/10.1103/RevModPhys.75.1085

Hasegawa, M., Hirose, K., Oka, K., & Ohishi, Y. (2021). Liquidus phase relations and solid-liquid partitioning in the Fe-Si-C system under core pressures. Geophysical Research Letters, 48(13), e2021GL092681. https://doi.org/10.1029/2021GL092681

He, Y., Sun, S., Kim, D. Y., Jang, B. G., Li, H., & Mao, H. K. (2022). Superionic iron alloys and their seismic velocities in Earth's inner core. Nature, 602(7896), 258-262. https://doi.org/10.1038/s41586-021-04361-x

Hirose, K., Morard, G., Sinmyo, R., Umemoto, K., Hernlund, J., Helffrich, G., & Labrosse, S. (2017). Crystallization of silicon dioxide and compositional evolution of the Earth's core. Nature, 543(7643), 99-102. https://doi.org/10.1038/nature21367

Hirose, K., Wood, B., & Vočadlo, L. (2021). Light elements in the Earth's core. Nature Reviews Earth & Environment, 2(9), 645-658. https://doi.org/10.1038/s43017-021-00203-6

Huguet, L., Van Orman, J. A., Hauck II, S. A., & Willard, M. A. (2018). Earth's inner core nucleation paradox. Earth and Planetary Science Letters, 487, 9-20. https://doi.org/10.1016/j.epsl.2018.01.018

Inoue, H., Suehiro, S., Ohta, K., Hirose, K., & Ohishi, Y. (2020). Resistivity saturation of hcp Fe-Si alloys in an internally heated diamond anvil cell: A key to assessing the Earth's core conductivity. Earth and Planetary Science Letters, 543, 116357. https://doi.org/10.1016/j.epsl.2020.116357

Ishii, M., & Dziewoński, A. M. (2002). The innermost inner core of the earth: Evidence for a change in anisotropic behavior at the radius of about 300 km. Proceedings of the National Academy of Sciences, 99(22), 14026-14030. https://doi.org/10.1073/pnas.172508499

Jeanloz, R., & Wenk, H. R. (1988). Convection and anisotropy of the inner core. Geophysical Research Letters, 15(1), 72-75. https://doi.org/10.1029/GL015i001p00072

Kleinschmidt, U., French, M., Steinle-Neumann, G., & Redmer, R. (2023). Electrical and thermal conductivity of fcc and hcp iron under conditions of the Earth's core from ab initio simulations. Physical Review B, 107(8), 085145. https://doi.org/10.1103/PhysRevB.107.085145

Kou, S., & Akai, H. (2018). First-principles calculation of transition-metal Seebeck coefficients. Solid State Communications, 276, 1-4. https://doi.org/10.1016/j.ssc.2018.02.018

Kuwayama, Y., Hirose, K., Sata, N., & Ohishi, Y. (2008). Phase relations of iron and iron–nickel alloys up to 300 GPa: Implications for composition and structure of the Earth's inner core. Earth and Planetary Science Letters, 273(3-4), 379-385. https://doi.org/10.1016/j.epsl.2008.07.001

Labrosse, S. (2014). Thermal and compositional stratification of the inner core. Comptes Rendus Geoscience, 346(5-6), 119-129. https://doi.org/10.1016/j.crte.2014.04.005

Lasbleis, M., & Deguen, R. (2015). Building a regime diagram for the Earth's inner core. Physics of the Earth and Planetary Interiors, 247, 80-93. https://doi.org/10.1016/j.pepi.2015.02.001

Lasbleis, M., Kervazo, M., & Choblet, G. (2020). The fate of liquids trapped during the Earth's inner core growth. Geophysical Research Letters, 47(2), e2019GL085654. https://doi.org/10.1029/2019GL085654

Lenhart, E. M., & Secco, R. A. (2022). Implications for the energy source for an early dynamo in Vesta from experiments on electrical resistivity of liquid Fe-10wt% Ni at high pressures. Icarus, 378, 114962. https://doi.org/10.1016/j.icarus.2022.114962

Lenhart, E. M., Yong, W., Secco, R. A., & Flemming, R. (2023). Electrical resistivity of liquid Fe-8wt% S-4.5 wt% Si at high pressures with implications for heat flux through the cores of Io and sub-earth exoplanets. Icarus, 395, 115472. https://doi.org/10.1016/j.icarus.2023.115472

Li, X., & Cormier, V. F. (2002). Frequency-dependent seismic attenuation in the inner core, 1. A viscoelastic interpretation. Journal of Geophysical Research: Solid Earth, 107(B12), ESE-13. https://doi.org/10.1029/2002JB001795

Li, Y., Vočadlo, L., & Brodholt, J. P. (2018). The elastic properties of hcp-Fe alloys under the conditions of the Earth’s inner core. Earth and Planetary Science Letters, 493, 118-127. https://doi.org/10.1016/j.epsl.2018.04.013

Littleton, J. A., Secco, R. A., & Yong, W. (2021a). Electrical resistivity of FeS at high pressures and temperatures: Implications of thermal transport in the core of Ganymede. Journal of Geophysical Research: Planets, 126(5), e2020JE006793. https://doi.org/10.1029/2020JE006793

Littleton, J. A., Secco, R. A., & Yong, W. (2021b). Thermal convection in the core of Ganymede inferred from liquid eutectic Fe-FeS electrical resistivity at high pressures. Crystals, 11(8), 875. https://doi.org/10.3390/cryst11080875

Littleton, J. A., Yong, W., & Secco, R. A. (2022). Electrical resistivity of the Fe–Si–S ternary system: implications for timing of thermal convection shutdown in the lunar core. Scientific Reports, 12(1), 19031. https://doi.org/10.1038/s41598-022-21904-y

Lythgoe, K. H., Rudge, J. F., Neufeld, J. A., & Deuss, A. (2015). The feasibility of thermal and compositional convection in Earth's inner core. Geophysical Journal International, 201(2), 764-782. https://doi.org/10.1093/gji/ggv034

Manthilake, G., Chantel, J., Monteux, J., Andrault, D., Bouhifd, M. A., Bolfan Casanova, N., Boulard, E., Guignot, N., King, A., & Itié, J. P. (2019). Thermal conductivity of FeS and its implications for Mercury's long-sustaining magnetic field. Journal of Geophysical Research: Planets, 124(9), 2359-2368. https://doi.org/10.1029/2019JE005979

Markowitz, D. (1977). Calculation of electrical resistivity of highly resistive metallic alloys. Physical Review B, 15(8), 3617. https://doi.org/10.1103/PhysRevB.15.3617

Martorell, B., Vočadlo, L., Brodholt, J., & Wood, I. G. (2013). Strong premelting effect in the elastic properties of hcp-Fe under inner-core conditions. Science, 342(6157), 466-468. https://doi.org/10.1126/science.1243651

Momma, K., & Izumi, F. (2011). VESTA 3 for three-dimensional visualization of crystal, volumetric and morphology data. Journal of applied crystallography, 44(6), 1272-1276. https://doi.org/10.1107/S0021889811038970

Monnereau, M., Calvet, M., Margerin, L., & Souriau, A. (2010). Lopsided growth of Earth’s inner core. Science, 328(5981), 1014-1017. https://doi.org/10.1126/science.1186212

Mookherjee, M., Nakajima, Y., Steinle-Neumann, G., Glazyrin, K., Wu, X., Dubrovinsky, L., McCammon, C., & Chumakov, A. (2011). High-pressure behavior of iron carbide (Fe7C3) at inner core conditions. Journal of Geophysical Research: Solid Earth, 116(B4). https://doi.org/10.1029/2010JB007819

Moruzzi, V.L., Janak, J.F., & Williams, A.R., (1978). Calculated electronic properties of metals.

Nadal, M. H., & Le Poac, P. (2003). Continuous model for the shear modulus as a function of pressure and temperature up to the melting point: analysis and ultrasonic validation. Journal of applied physics, 93(5), 2472-2480. https://doi.org/10.1063/1.1539913

O'Rourke, J. G., & Stevenson, D. J. (2016). Powering Earth's dynamo with magnesium precipitation from the core. Nature, 529(7586), 387-389. https://doi.org/10.1038/nature16495

Ohta, K., Kuwayama, Y., Hirose, K., Shimizu, K., & Ohishi, Y. (2016). Experimental determination of the electrical resistivity of iron at Earth's core conditions. Nature, 534(7605), 95-98. https://doi.org/10.1038/nature17957

Ohta, K., Nishihara, Y., Sato, Y., Hirose, K., Yagi, T., Kawaguchi, S. I., Hirao, N., & Ohishi, Y. (2018). An experimental examination of thermal conductivity anisotropy in hcp iron. Frontiers in Earth Science, 6, 176. https://doi.org/10.3389/feart.2018.00176

Ohta, K., Suehiro, S., Hirose, K., & Ohishi, Y. (2019). Electrical resistivity of fcc phase iron hydrides at high pressures and temperatures. Comptes Rendus Geoscience, 351(2-3), 147-153. https://doi.org/10.1016/j.crte.2018.05.004

Orole, O. A., Yong, W., & Secco, R. A. (2022). Thermal Convection in Vesta's Core from Experimentally-Based Conductive Heat Flow Estimates. Crystals, 12(12), 1752. https://doi.org/10.3390/cryst12121752

Oshita, M., Yotsuhashi, S., Adachi, H., & Akai, H. (2009). Seebeck coefficient calculated by kubo–greenwood formula on the basis of density functional theory. Journal of the Physical Society of Japan, 78(2), 024708-024708. https://doi.org/10.1143/jpsj.78.024708

Ouzounis, A., & Creager, K. C. (2001). Isotropy overlying anisotropy at the top of the inner core. Geophysical research letters, 28(22), 4331-4334. https://doi.org/10.1029/2001GL013341

Phạm, T. S., & Tkalčić, H. (2023). Up-to-fivefold reverberating waves through the Earth's center and distinctly anisotropic innermost inner core. Nature Communications, 14(1), 754. https://doi.org/10.1038/s41467-023-36074-2

Pommier, A. (2018). Influence of sulfur on the electrical resistivity of a crystallizing core in small terrestrial bodies. Earth and Planetary Science Letters, 496, 37-46. https://doi.org/10.1016/j.epsl.2018.05.032

Pommier, A. (2020). Experimental investigation of the effect of nickel on the electrical resistivity of Fe-Ni and Fe-Ni-S alloys under pressure. American Mineralogist, 105(7), 1069-1077. https://doi.org/10.2138/am-2020-7301

Pommier, A., Leinenweber, K., & Tran, T. (2019). Mercury's thermal evolution controlled by an insulating liquid outermost core?. Earth and Planetary Science Letters, 517, 125-134. https://doi.org/10.1016/j.epsl.2019.04.022

Pourovskii, L. V., Mravlje, J., Georges, A., Simak, S. I., & Abrikosov, I. A. (2017). Electron–electron scattering and thermal conductivity of ϵ-iron at Earth's core conditions. New Journal of Physics, 19(7), 073022. https://doi.org/10.1088/1367-2630/aa76c9

Pozzo, M., & Alfè, D. (2016). Saturation of electrical resistivity of solid iron at Earth's core conditions. SpringerPlus, 5, 1-6. https://doi.org/10.1186/s40064-016-1829-x

Pozzo, M., Davies, C., Gubbins, D., & Alfè, D. (2014). Thermal and electrical conductivity of solid iron and iron–silicon mixtures at Earth's core conditions. Earth and Planetary Science Letters, 393, 159-164. https://doi.org/10.1016/j.epsl.2014.02.047

Ramakrishna, K., Lokamani, M., Baczewski, A., Vorberger, J., & Cangi, A. (2023). Electrical conductivity of iron in Earth's core from microscopic Ohm's law. Physical Review B, 107(11), 115131. https://doi.org/10.1103/PhysRevB.107.115131

Ramakrishna, K., Lokamani, M., Baczewski, A., Vorberger, J., & Cangi, A. (2022). Electrical and Thermal Conductivity of High-Pressure Solid Iron. arXiv preprint arXiv:2210.10132. https://doi.org/10.48550/arXiv.2210.10132

Song, X., & Helmberger, D. V. (1995). Depth dependence of anisotropy of Earth's inner core. Journal of Geophysical Research: Solid Earth, 100(B6), 9805-9816. https://doi.org/10.1029/95JB00244

Spedding, F. H., Cress, D., & Beaudry, B. J. (1971). The resistivity of scandium single crystals. Journal of the Less Common Metals, 23(3), 263-270. https://doi.org/10.1016/0022-5088(71)90140-8

Stephenson, J., Tkalčić, H., & Sambridge, M. (2021). Evidence for the innermost inner core: Robust parameter search for radially varying anisotropy using the neighborhood algorithm. Journal of Geophysical Research: Solid Earth, 126(1), e2020JB020545. https://doi.org/10.1029/2020JB020545

Suehiro, S., Ohta, K., Hirose, K., Morard, G., & Ohishi, Y. (2017). The influence of sulfur on the electrical resistivity of hcp iron: Implications for the core conductivity of Mars and Earth. Geophysical Research Letters, 44(16), 8254-8259. https://doi.org/10.1002/2017GL074021

Suehiro, S., Wakamatsu, T., Ohta, K., Hirose, K., & Ohishi, Y. (2019). High-temperature electrical resistivity measurements of hcp iron to Mbar pressure in an internally resistive heated diamond anvil cell. High Pressure Research, 39(4), 579-587. https://doi.org/10.1080/08957959.2019.1692008

Sundqvist, B. (2022). Resistivity saturation in crystalline metals: Semi-classical theory versus experiment. Journal of Physics and Chemistry of Solids, 165, 110686. https://doi.org/10.1016/j.jpcs.2022.110686

Tanaka, S., & Hamaguchi, H. (1997). Degree one heterogeneity and hemispherical variation of anisotropy in the inner core from PKP (BC)–PKP (DF) times. Journal of Geophysical Research: Solid Earth, 102(B2), 2925-2938. https://doi.org/10.1029/96JB03187

Tateno, S., Kuwayama, Y., Hirose, K., & Ohishi, Y. (2015). The structure of Fe–Si alloy in Earth's inner core. Earth and Planetary Science Letters, 418, 11-19. https://doi.org/10.1016/j.epsl.2015.02.008

Vočadlo, L., Alfe, D., Gillan, M. J., & Price, G. D. (2003). The properties of iron under core conditions from first principles calculations. Physics of the Earth and Planetary Interiors, 140(1-3), 101-125. https://doi.org/10.1016/j.pepi.2003.08.001

Wang, W., Li, Y., Brodholt, J. P., Vočadlo, L., Walter, M. J., & Wu, Z. (2021). Strong shear softening induced by superionic hydrogen in Earth's inner core. Earth and Planetary Science Letters, 568, 117014. https://doi.org/10.1016/j.epsl.2021.117014

Weber, P., & Machetel, P. (1992). Convection within the inner-core and thermal implications. Geophysical Research Letters, 19(21), 2107-2110. https://doi.org/10.1029/92GL02148

Xu, J., Zhang, P., Haule, K., Minar, J., Wimmer, S., Ebert, H., & Cohen, R. E. (2018). Thermal conductivity and electrical resistivity of solid iron at Earth's core conditions from first principles. Physical Review Letters, 121(9), 096601. https://doi.org/10.1103/PhysRevLett.121.096601

Yamauchi, H., & Takei, Y. (2016). Polycrystal anelasticity at near-solidus temperatures. Journal of Geophysical Research: Solid Earth, 121(11), 7790-7820. https://doi.org/10.1002/2016JB013316

Yamauchi, H., & Takei, Y. (2020). Application of a premelting model to the lithosphere-asthenosphere boundary. Geochemistry, Geophysics, Geosystems, 21(11), e2020GC009338. https://doi.org/10.1029/2020GC009338

Yang, H., Muir, J. M., & Zhang, F. (2022). Iron hydride in the Earth's inner core and its geophysical implications. Geochemistry, Geophysics, Geosystems, e2022GC010620. https://doi.org/10.1029/2022GC010620

Yin, Y., Wang, L., Zhai, S., & Fei, Y. (2022). Electrical Resistivity of Fe and Fe-3 wt% P at 5 GPa With Implications for the Moon's Core Conductivity and Dynamo. Journal of Geophysical Research: Planets, 127(4), e2021JE007116. https://doi.org/10.1029/2021JE007116

Yukutake, T. (1998). Implausibility of thermal convection in the Earth’s solid inner core. Physics of the Earth and Planetary Interiors, 108(1), 1-13. https://doi.org/10.1016/S0031-9201(98)00097-1

Zhang, C., Lin, J. F., Liu, Y., Feng, S., Jin, C., Hou, M., & Yoshino, T. (2018). Electrical resistivity of Fe-C alloy at high pressure: Effects of carbon as a light element on the thermal conductivity of the Earth’s core. Journal of Geophysical Research: Solid Earth, 123(5), 3564-3577. https://doi.org/10.1029/2017JB015260

Zhang, Y., Hou, M., Liu, G., Zhang, C., Prakapenka, V. B., Greenberg, E., Fei, Y., Cohen, R.E., & Lin, J. F. (2020a). Reconciliation of experiments and theory on transport properties of iron and the geodynamo. Physical review letters, 125(7), 078501. https://doi.org/10.1103/PhysRevLett.125.078501

Zhang, Y., Luo, K., Hou, M., Driscoll, P., Salke, N. P., Minár, J., Prakapenka, V.B., Greenberg, E., Hemley, R.J., Cohen, R.E., & Lin, J. F. (2022). Thermal conductivity of Fe-Si alloys and thermal stratification in Earth’s core. Proceedings of the National Academy of Sciences, 119(1), e2119001119. https://doi.org/10.1073/pnas.2119001119

Zhang, Z., Csányi, G., & Alfè, D. (2020b). Partitioning of sulfur between solid and liquid iron under Earth’s core conditions: Constraints from atomistic simulations with machine learning potentials. Geochimica et Cosmochimica Acta, 291, 5-18. https://doi.org/10.1016/j.gca.2020.03.028

Zidane, M., Salmani, E. M., Majumdar, A., Ez-Zahraouy, H., Benyoussef, A., & Ahuja, R. (2020). Electrical and thermal transport properties of Fe–Ni based ternary alloys in the earth's inner core: An ab initio study. Physics of the Earth and Planetary Interiors, 301, 106465. https://doi.org/10.1016/j.pepi.2020.106465

Acknowledgements

This work was supported by JSPS MEXT/KAKENHI Grant Number 20K22365, 22K03754, and 21H04968.

Data Availability Statement

Datasets for this study are available online https://doi.org/10.5281/zenodo.7929259.

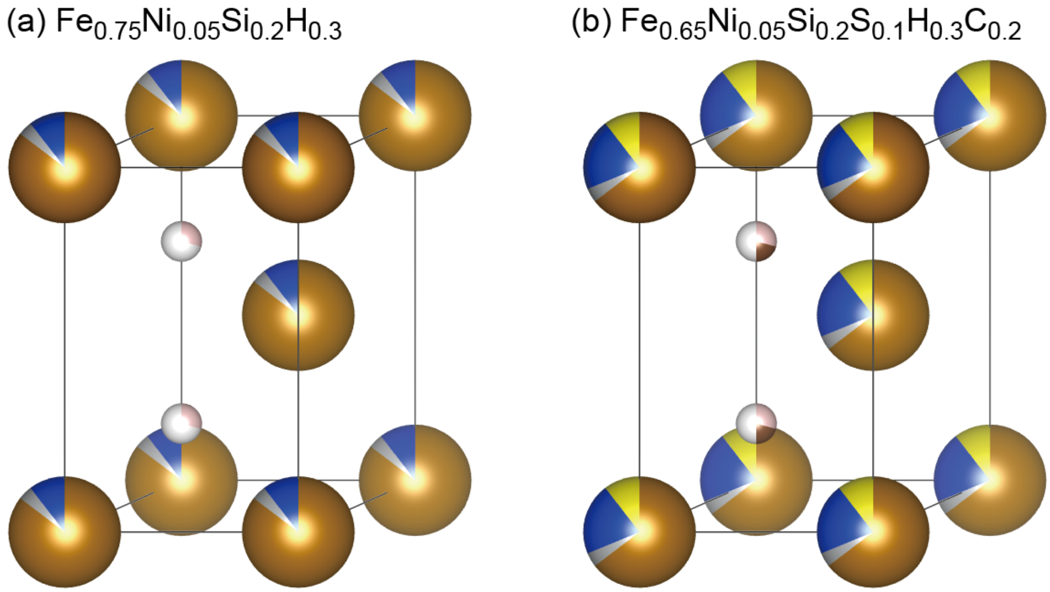

Figure 1. The crystal structure of hcp Fe-based alloy is illustrated using the VESTA program (Momma & Izumi, 2011). (a) $Fe_{0.75}Ni_{0.05}Si_{0.2}H_{0.3}$ alloy, which is an example of a 4-component alloy. Ni (silver) and Si (blue) enter the substitutional site of hcp Fe (brown), whereas H (pink) occupies the octahedral interstitial site. (b) $Fe_{0.65}Ni_{0.05}Si_{0.2}S_{0.1}H_{0.3}C_{0.2}$ alloy, which is an example of a 6-component alloy. Note that Ni, Si, and S (yellow) enter the substitutional site simultaneously, and H and C (dark brown) are simultaneously located at the interstitial site.

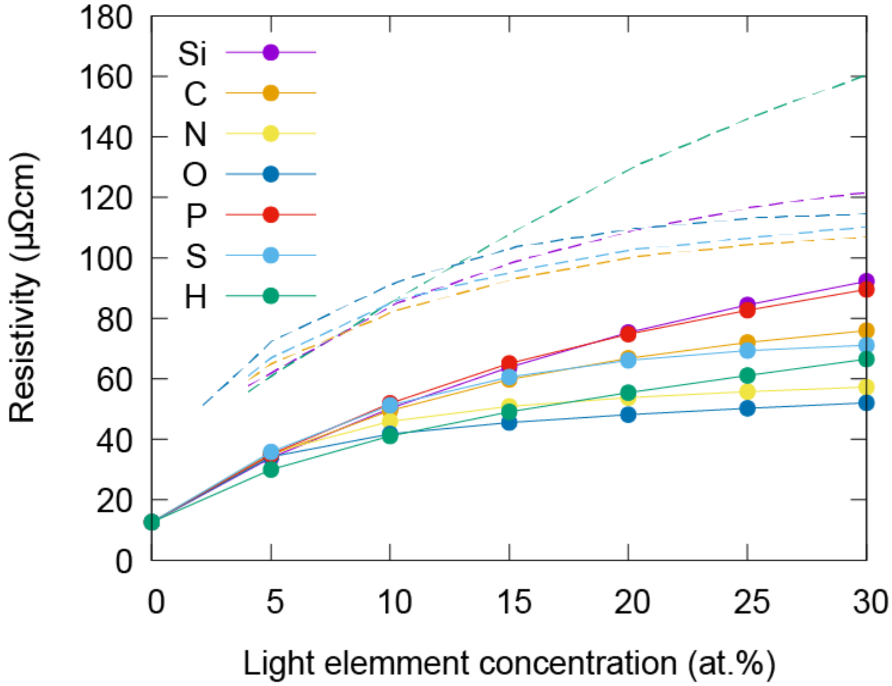

Figure 2. The resistivity of hcp $Fe_{0.9-x}Ni_{0.1}L^{i}_{x}$ substitutional ternary alloys. Substitutional light element is Si (purple), C (orange), N (yellow), O (blue), P (red), S (cyan), or H (green). Solid lines with circles are present calculations. Broken lines are previous calculations (Zidane et al., 2020). Note that Zidane et al. (2020) overestimated the resistivity.

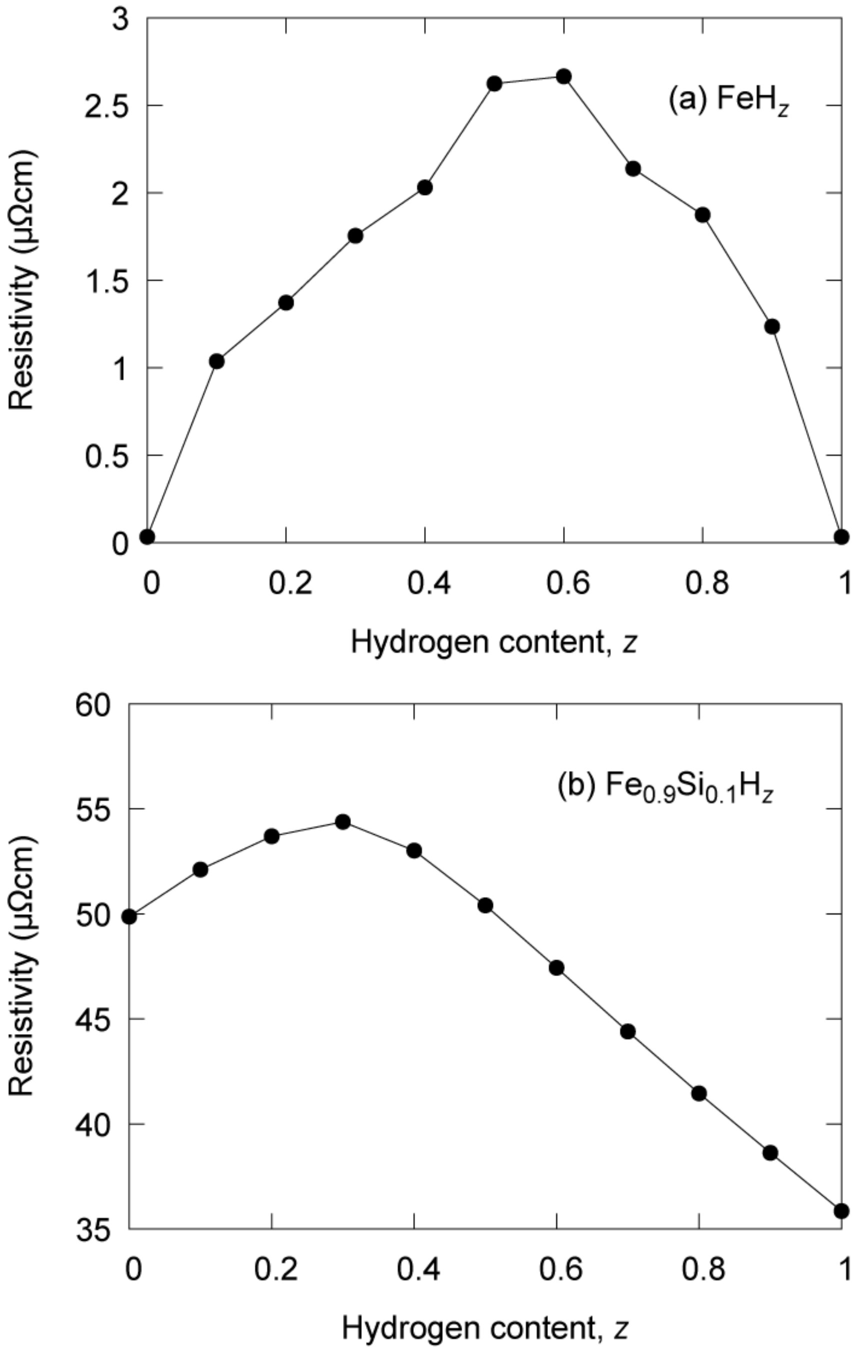

Figure 3. The resistivity of hcp (a) FeH$_z$ (b) $Fe_{0.95}Ni_{0.05}H_z$, and (c) $Fe_{0.9}Si_{0.1}H_z$ alloys as functions of H content, z.

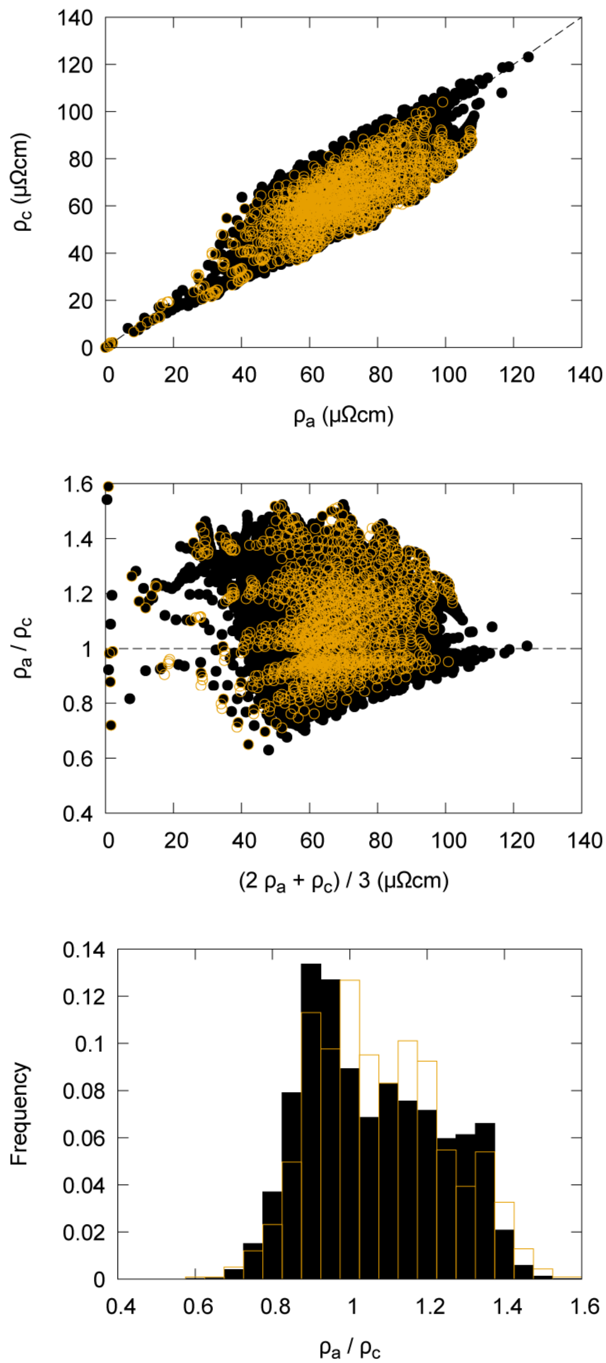

Figure 4. Anisotropic impurity resistivity of hcp Fe-based alloys with 4- (black) and 6-component (orange) alloys. (a) impurity resistivity parallel (ρ_c) and perpendicular (ρ_a) to the *c*-axis. (b) Resistivity ratio. (c) Histogram of the resistivity ratio (ρ_a / ρ_c).

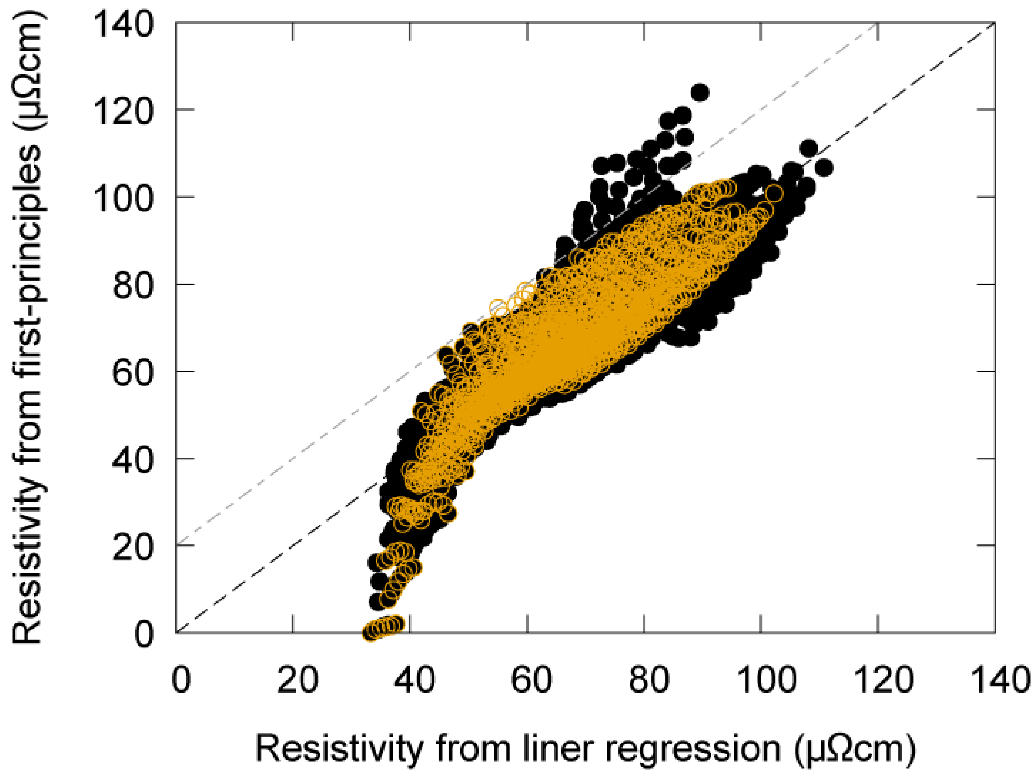

Figure 5. Result of the linear regression for 4-component alloys (black filled circle). 6-component alloys (orange open circle) are consistent with 4-component alloys. Black broken line indicates the regression line, and gray dotted-broken line represents the resistivity 20 μΩcm higher than the regression line.

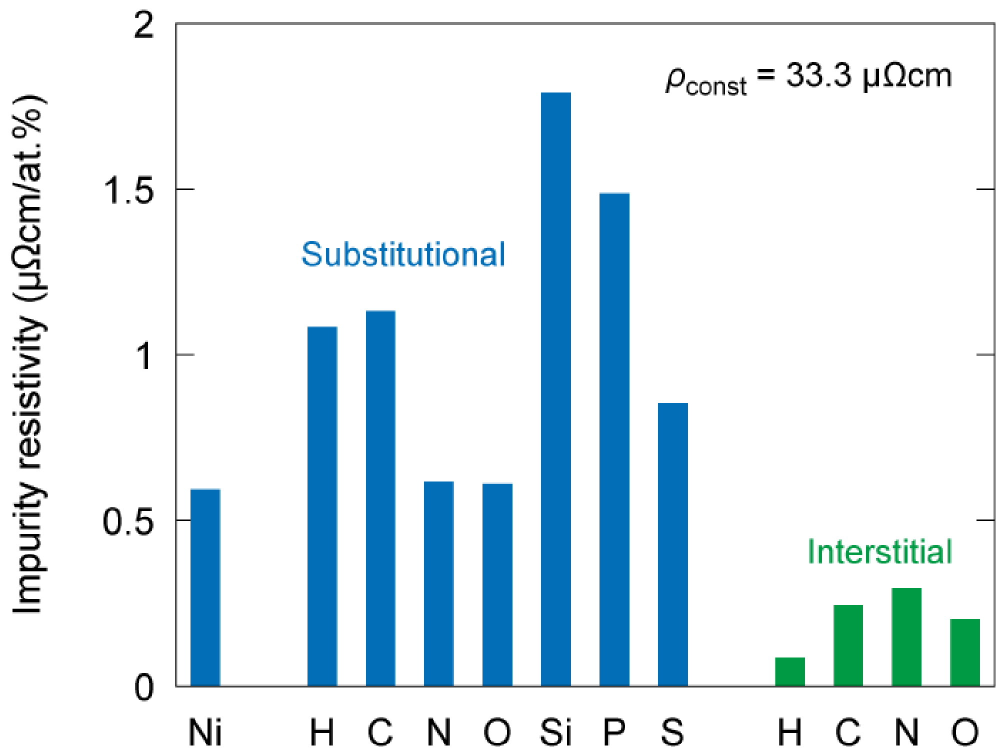

Figure 6. Regression coefficients for the impurity resistivity 4-component alloys. Substitutional impurities are indicated as blue and interstitial impurites are green.

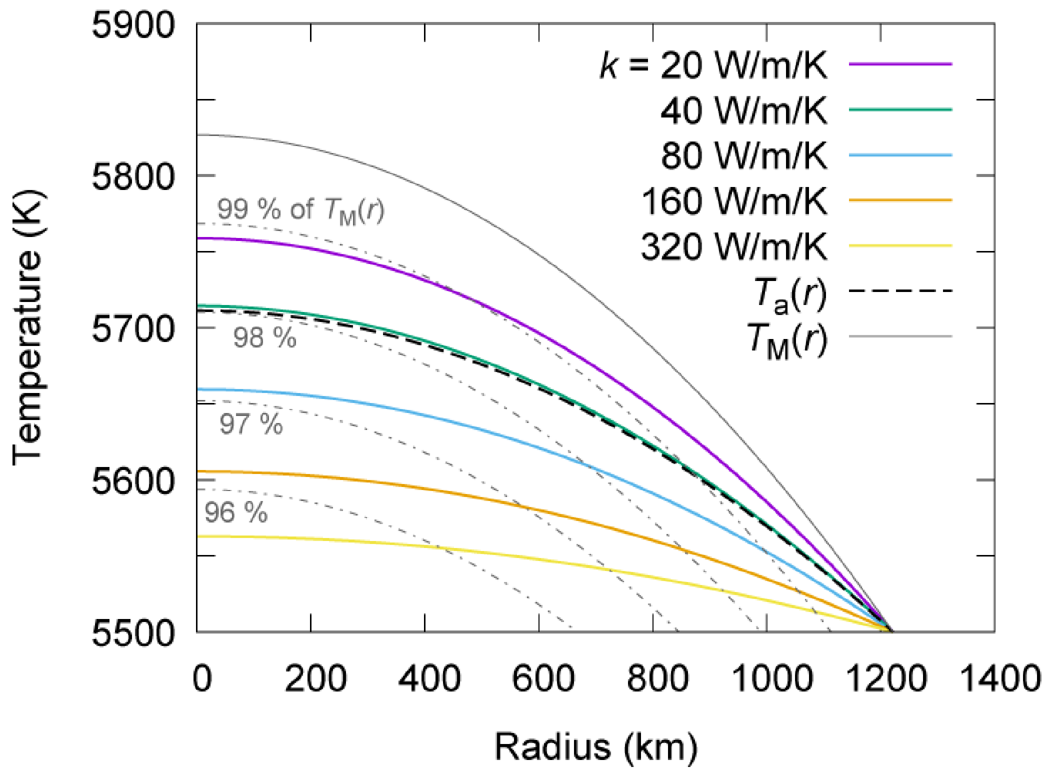

Figure 7. The present-day temperature profile within the inner core with the inner-core age of 1 Gyr. Thick solid lines indicate the conductive temperature profile with thermal conductivity of 20 (purple), 40 (green), 80 (cyan), 160 (orange), and 320 W/m/K (yellow). The broken line represents the adiabatic temperature profile. For thermal convection to occur, the temperature must be higher than the adiabat. The solid gray line represents the melting temperature. Gray dotted broken lines are 99, 98, 97, and 96 % of the melting temperature.

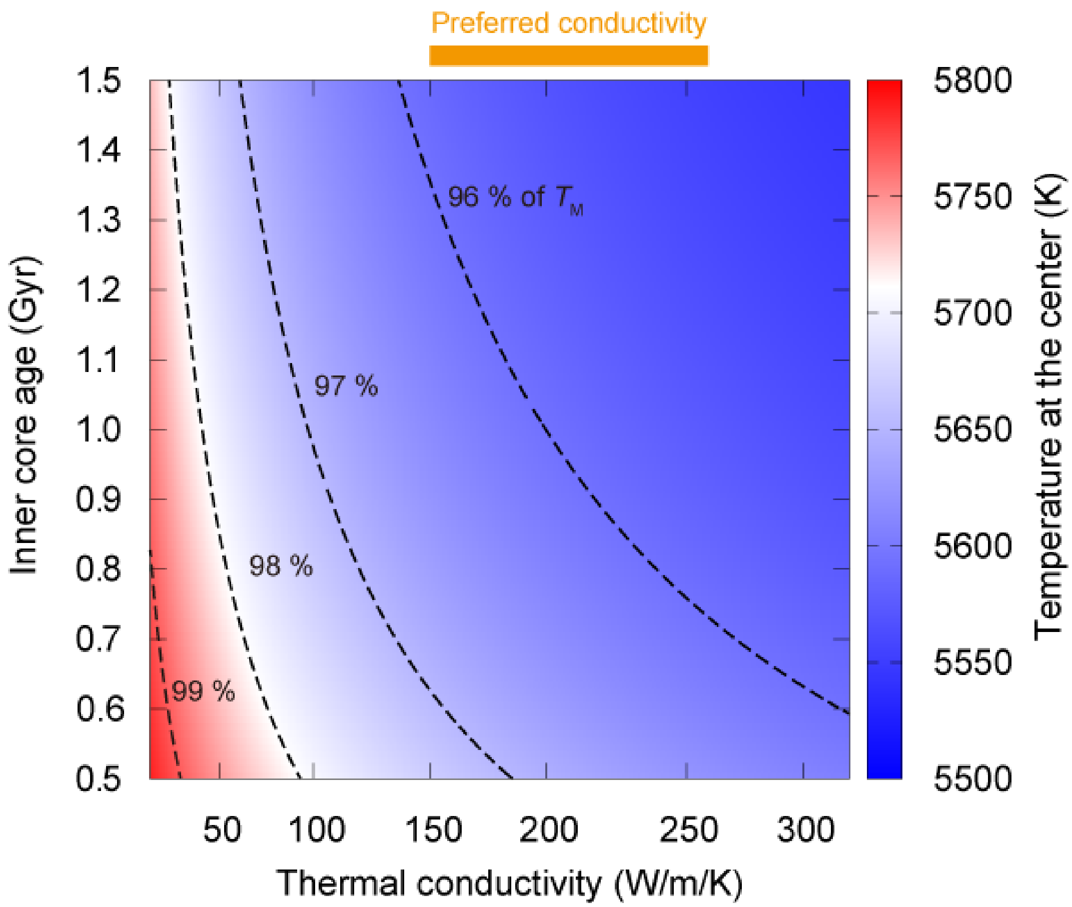

Figure 8. The present-day temperature at the center of the inner core as a function of thermal conductivity and inner-core age. The red region indicates thermal instability, whereas the blue area tends to become thermal stratification. Broken lines are iso-temperature curves corresponding to 99, 98, 97, and 96 % of the melting temperature. The preferred thermal conductivity range (150-263 W/m/K) is indicated as the orange band.

Figure 1.

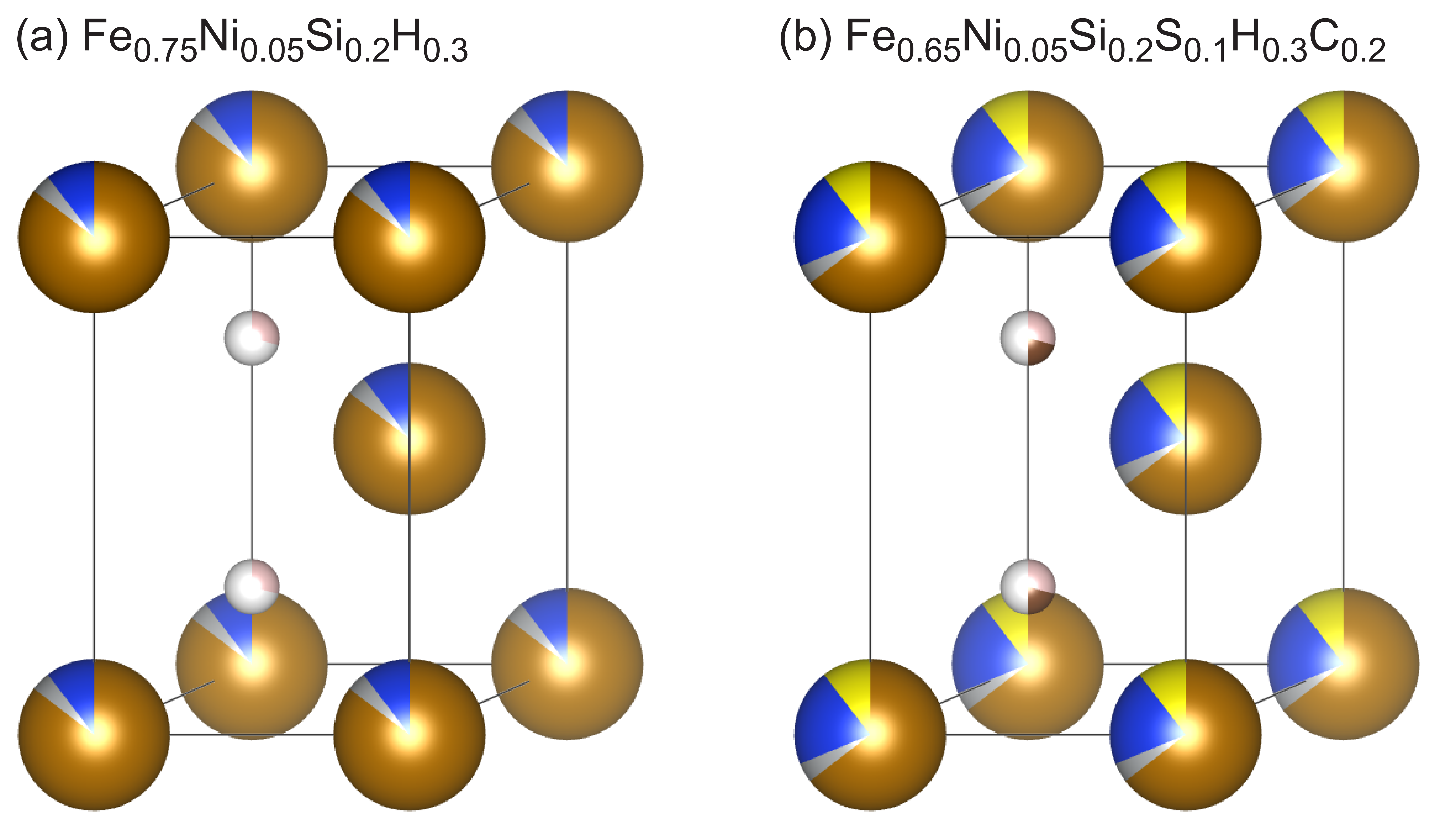
(a) $Fe_{0.75}Ni_{0.05}Si_{0.2}H_{0.3}$
(b) $Fe_{0.65}Ni_{0.05}Si_{0.2}S_{0.1}H_{0.3}C_{0.2}$

Figure 2.

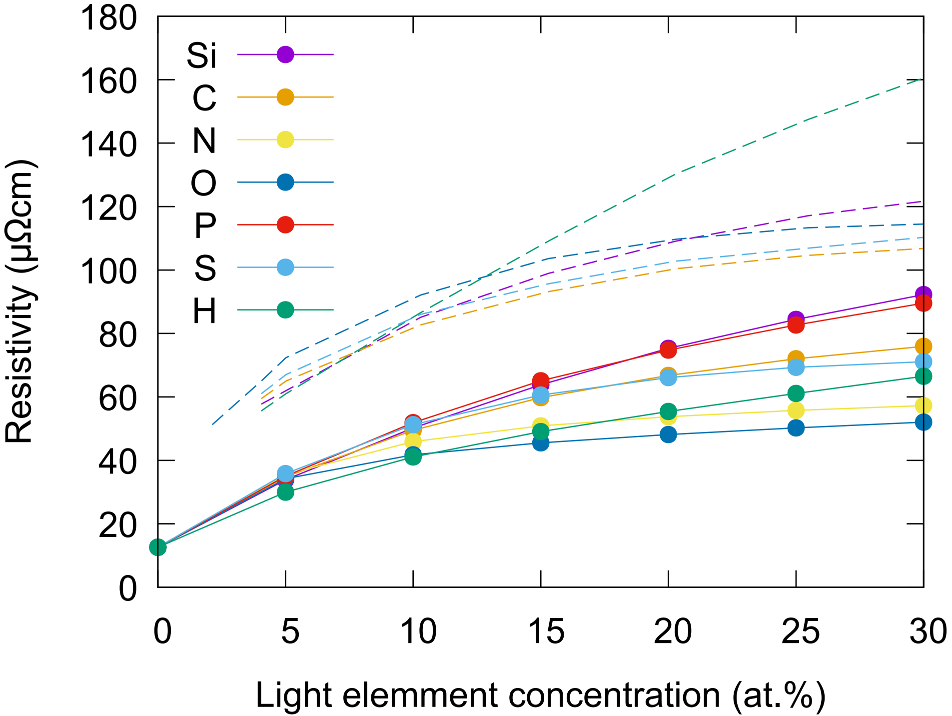

Resistivity (μΩcm)
Light elemment concentration (at.%)
Si
C
N
O
P
S
H
0
20
40
60
80
100
120
140
160
180
0
5
10
15
20
25
30

Figure 3.

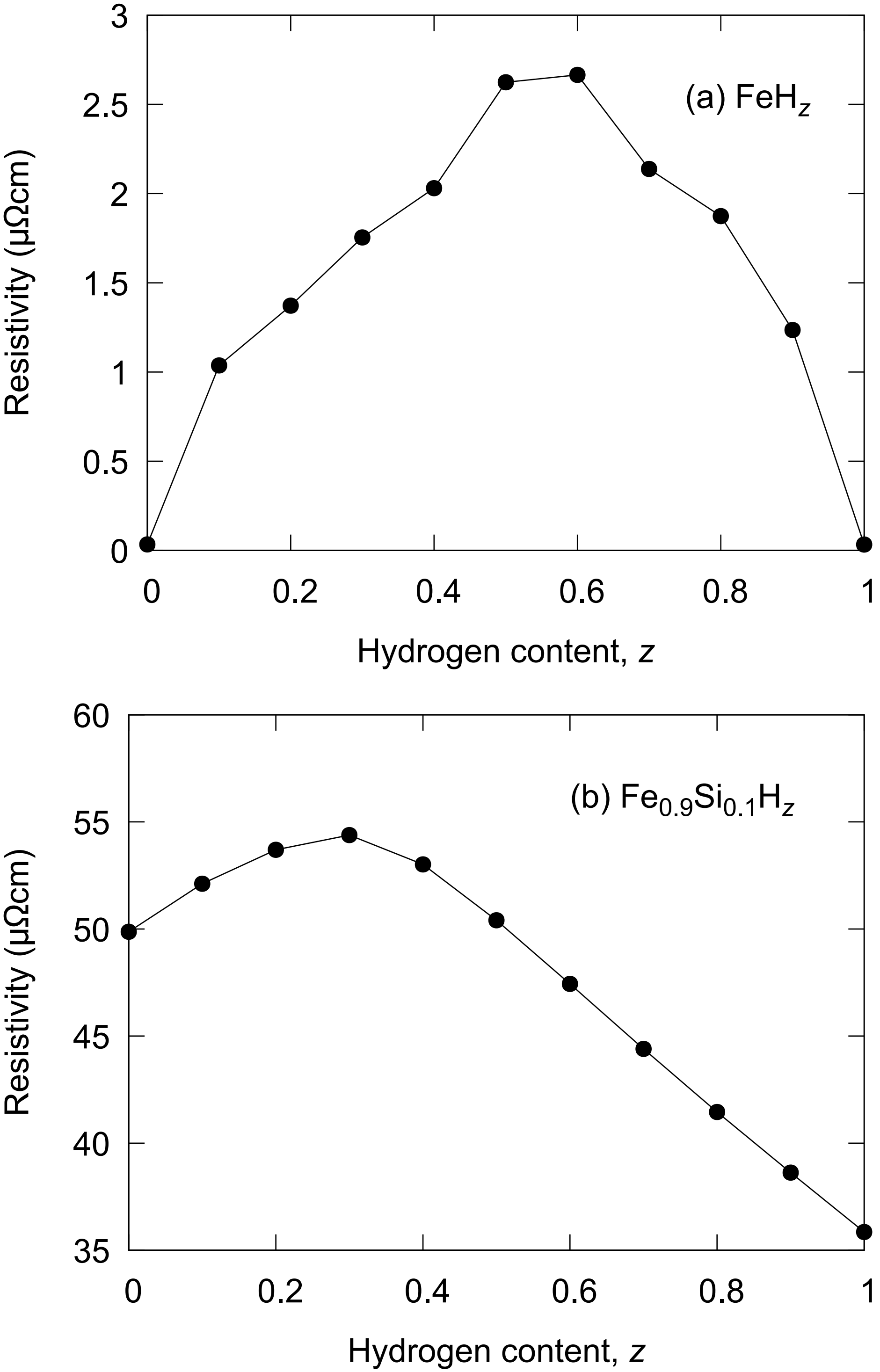
(a) FeH_z
Resistivity (μΩcm)
Hydrogen content, z
0
0.5
1
1.5
2
2.5
3
0
0.2
0.4
0.6
0.8
1
(b) $Fe_{0.9}Si_{0.1}H_z$
Resistivity (μΩcm)
Hydrogen content, z
35
40
45
50
55
60
0
0.2
0.4
0.6
0.8
1

Figure 4.

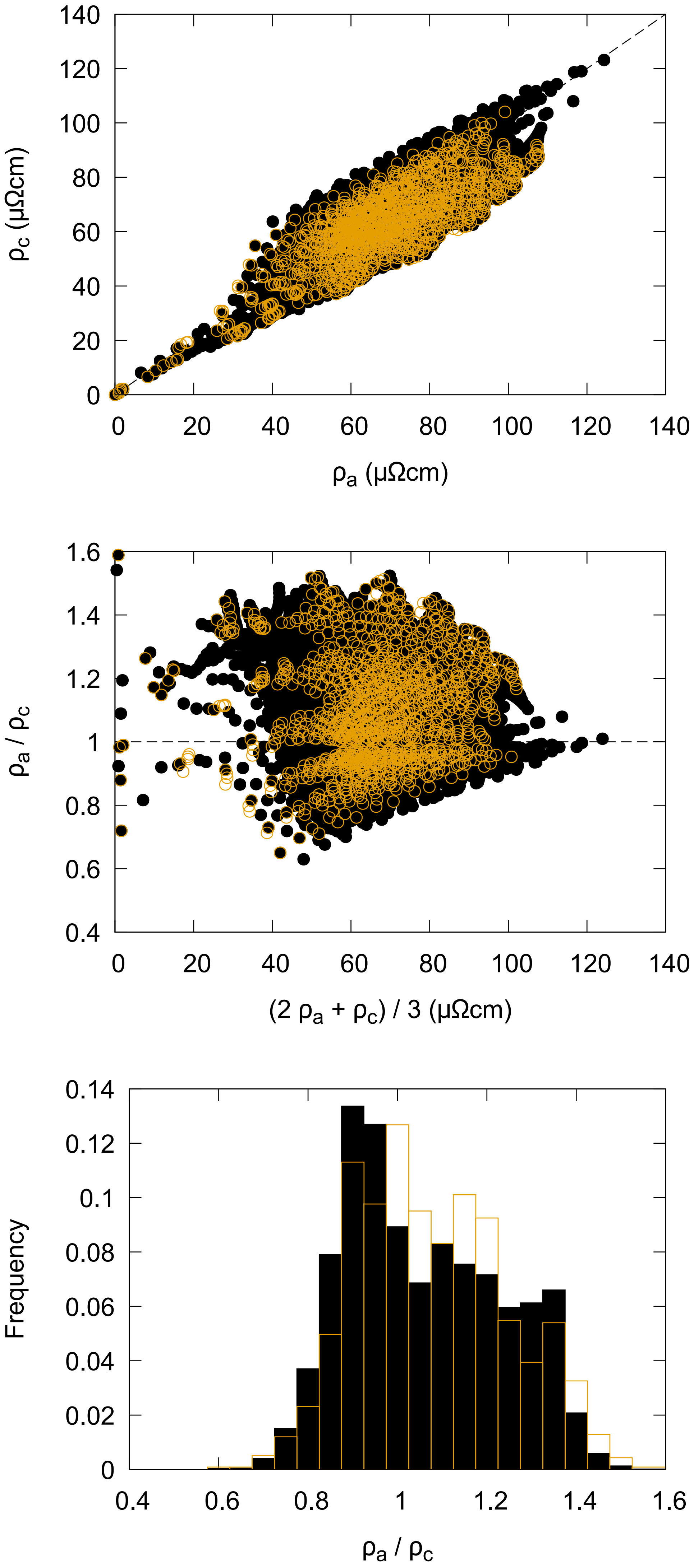

140
120
100
80
60
40
20
0
ρc (μΩcm)
0
20
40
60
80
100
120
140
ρa (μΩcm)
1.6
1.4
1.2
1
0.8
0.6
0.4
ρa / ρc
0
20
40
60
80
100
120
140
(2 ρa + ρc) / 3 (μΩcm)
0.14
0.12
0.1
0.08
0.06
0.04
0.02
0
Frequency
0.4
0.6
0.8
1
1.2
1.4
1.6
ρa / ρc

Figure 5.

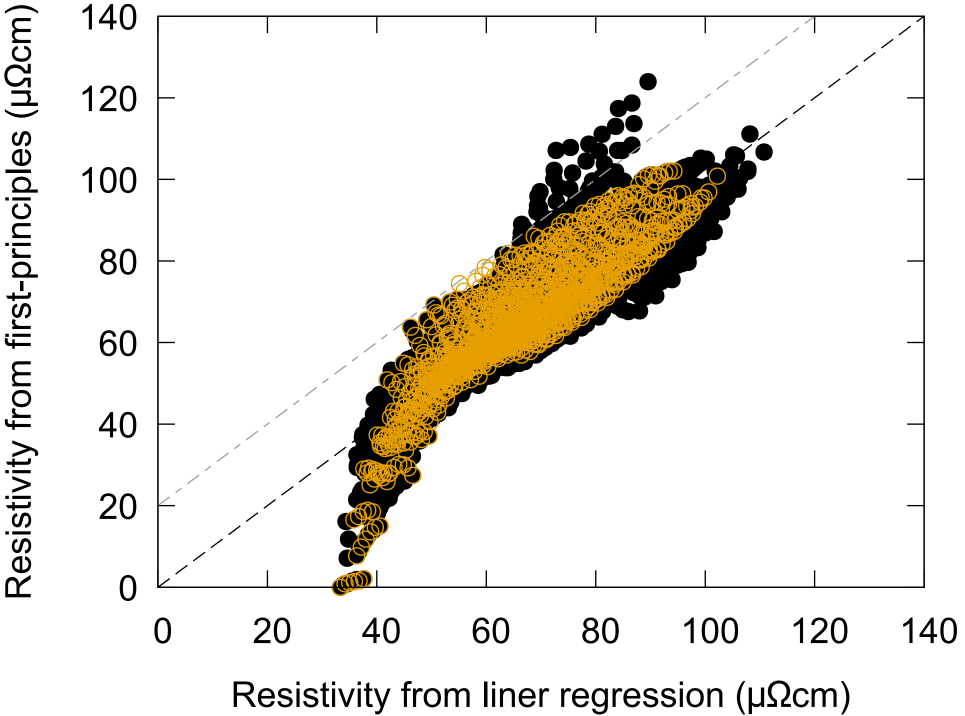

Resistivity from first-principles (μΩcm)
140
120
100
80
60
40
20
0
0
20
40
60
80
100
120
140
Resistivity from liner regression (μΩcm)

Figure 6.

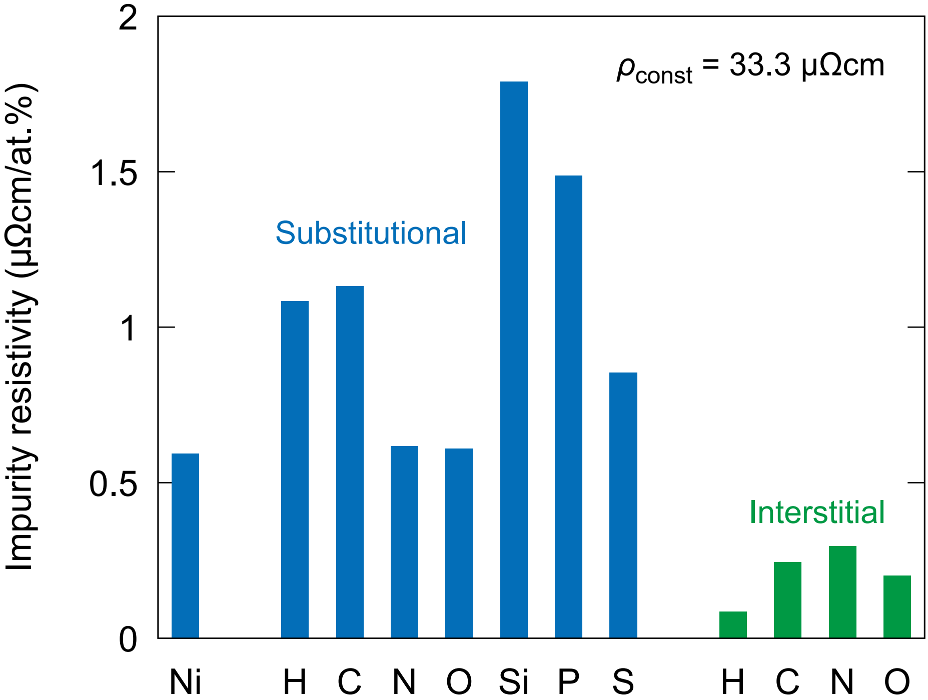

Impurity resistivity (μΩcm/at.%)
2
1.5
1
0.5
0
ρconst = 33.3 μΩcm
Substitutional
Interstitial
Ni
H
C
N
O
Si
P
S
H
C
N
O

Figure 7.

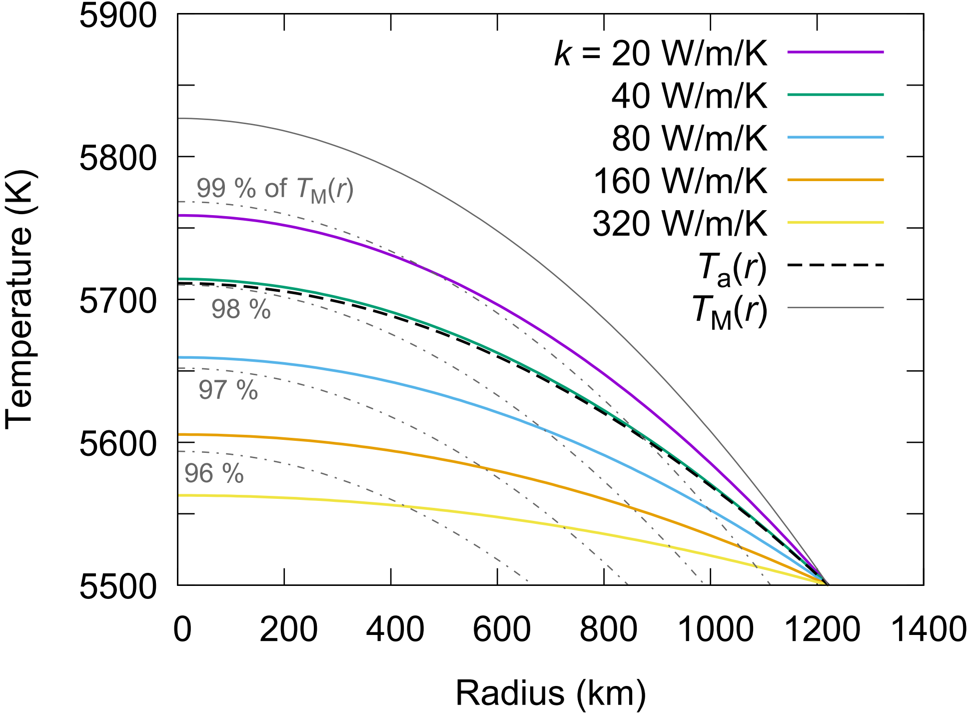

5900
5800
5700
5600
5500
0
200
400
600
800
1000
1200
1400
Temperature (K)
Radius (km)
k = 20 W/m/K
40 W/m/K
80 W/m/K
160 W/m/K
320 W/m/K
Ta(r)
TM(r)
99 % of TM(r)
98 %
97 %
96 %

Figure 8.

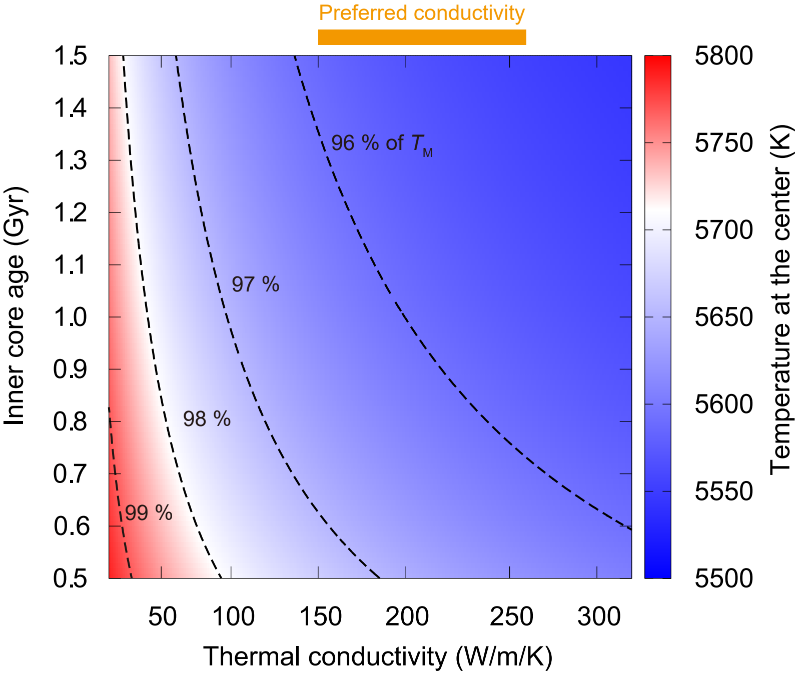

Preferred conductivity
1.5
1.4
1.3
1.2
1.1
1.0
0.9
0.8
0.7
0.6
0.5
Inner core age (Gyr)
96 % of T_M
97 %
98 %
99 %
50
100
150
200
250
300
Thermal conductivity (W/m/K)
5800
5750
5700
5650
5600
5550
5500
Temperature at the center (K)